

國立臺灣大學電機資訊學院電信工程學研究所

碩士論文

Graduate Institute of Communication Engineering
College of Electrical Engineering and Computer Science

National Taiwan University

Master Thesis

以耦合共振腔實現小型化枝幹耦合器之設計

Design of Compact Branch-Line Couplers with Coupled
Resonators



張維倫

Wei-Lun Chang

指導教授：吳瑞北 博士

Advisor: Ruey-Beei Wu, Ph.D.

中華民國 97 年 7 月

July, 2008



國立臺灣大學碩士學位論文
口試委員會審定書

以耦合共振腔實現小型化枝幹耦合器之設計

Design of Compact Branch-Line Couplers with Coupled
Resonators

本論文係張維倫君 (R94942017) 在國立臺灣大學電信工程學研究所完成之碩士學位論文，於民國九十六年六月二十三日承下列考試委員審查通過及口試及格，特此證明

口試委員：

吳端北

(簽名)

(指導教授)

陳仁強

王蒼岩

郭仁才

毛紹綱

系主任、所長

王峰

(簽名)



誌謝

兩年的碩班生活很快就結束了，首先要感謝指導教授吳瑞北老師，老師治學嚴謹學識豐富，經常可以一針見血地指出研究的缺失，除了研究以外，老師也教導了我們許多做人處事應有的態度。另外也要感謝口試委員陳俊雄教授、郭仁財教授、王蒼容教授及毛紹綱教授在口試時提供的寶貴意見，使得論文的內容更加完備。

除了教授之外，學長也在研究的路上提供了很多的幫助，黃定彝學長幫忙解決了很多理論上的問題，劉安錫學長在我決定論文題目的時候提供了很多個人的經驗及建議，而沈澤旻學長也提供了很多的幫助，解決實作及量測上的問題。

再來就是在同一間實驗室一同吃喝玩樂打電動的伙伴們，一同撐過兩年的邱老大，一起修課 meeting 的小錢、小燕子，AOC 強者八格，打拼事業的博程，要去美國的建賢，焊武帝君朋，認真的學長 A 宏，很罩的輝哥，很會打嘴炮的黎帥，一起打羽毛球的貓咪、皮琪，喜歡半夜去八里的至亨，還有小弘、皓哥、展裕、小郭、郭爸、飛機、槍王、蘇紀綱…族繁不及備載，希望大家未來都能順順利利。

最後要感謝爸媽無條件的支持，讓我順利完成碩士學業，也謝謝小啾的陪伴，使得兩年的碩士之旅，增添了許多色彩。謝謝你們。



摘要

本篇論文的主題是一種由耦合共振腔組成的枝幹耦合器。四分之一波長傳輸線可以等效成共振腔之間的耦合。因此，傳統的枝幹耦合器可以轉變成一個耦合共振腔網路。使用這種方法合成的耦合器會具有帶通的特性。此外，耦合器的面積會隨著共振腔的縮小而減少，相較於傳統的枝幹耦合器，利用微小化共振腔設計的耦合器可以省下百分之五十的面積。

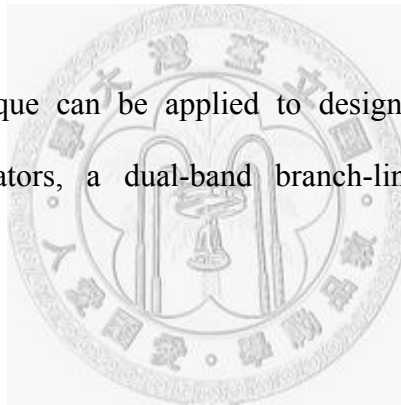
另外，這種方法也可以應用於設計雙頻的耦合器。配合步階式阻抗共振腔，可以得到一個具有帶通響應的雙頻枝幹耦合器。



Abstract

This thesis presents compact branch-line couplers composed of coupled resonators. The quarter-wavelength transmission lines are equivalent to the couplings between resonators. Therefore, the conventional branch-line coupler can be transformed into a coupled-resonator network. The resultant coupler provides bandpass characteristics. In addition, the size of coupler reduces as the size of resonator shrinks. With miniaturized resonators, the coupler saves 50% of area compared with conventional branch-line coupler.

Moreover, this technique can be applied to design dual-band couplers. With stepped-impedance resonators, a dual-band branch-line coupler with bandpass response is achieved.





Contents

Chapter 1 Introduction.....	1
1.1 Research Motivation	1
1.2 Literature Survey	1
1.3 Organization of the Thesis	3
Chapter 2 Basic Theory of Couplings	5
2.1 Basic Theory of Couplings	5
2.1.1 Electric Coupling	5
2.1.2 Magnetic Coupling.....	6
2.1.3 Mixed Coupling	7
2.1.4 External Quality Factor.....	9
2.2 Impedance and Admittance Inverters.....	10
Chapter 3 Analysis of Stepped-Impedance Resonators.....	13
3.1 Resonant Conditions	13
3.2 Characteristics of SIRs.....	15
3.3 Quarter-Wavelength SIRs	17
3.4 Net-Type Resonators.....	18
3.5 Designed Resonators.....	19
Chapter 4 Design of Compact Branch-Line Couplers with Coupled Resonators..	21
4.1 Equivalent Circuit of Branch-Line Coupler.....	22
4.2 Design of Branch-Line Couplers with Coupled Resonators.....	30
4.2.1 Coupler Design 1	30
4.2.2 Coupler Design 2	36
4.2.3 Coupler design 3	43
4.2.4 Coupler design 4	50
4.2.5 Dual-band coupler.....	56
Chapter 5 Conclusions.....	63
References	65



List of Tables

Table 4.1	Parameters of designed resonators (coupler design 2).....	39
Table 4.2	Parameters of designed resonators (coupler design 3).....	46
Table 4.3	Parameters of designed resonators (coupler design 4).....	52





List of Figures

Fig. 1.1. The concept of replacing quarter-wavelength transmission lines with the couplings between resonators	4
Fig. 2.1. (a) Coupled resonator circuit with electric coupling (b) An alternative form of the equivalent circuit	6
Fig. 2.2. (a) Coupled resonator circuit with magnetic coupling (b) An alternative form of the equivalent circuit.....	7
Fig. 2.3. An equivalent lumped-element circuit with both electric and magnetic couplings.....	8
Fig. 2.4. (a) Equivalent circuit of the I/O resonator with a single load (b) Phase response of S_{11}	10
Fig. 2.5. Impedance and admittance inverters (a) Operation of impedance and admittance inverters (b) Implementation as quarter-wave transformers (c) Implementation using transmission lines and reactive elements (d) Implementation using capacitor networks	11
Fig. 3.1. Structure of the stepped-impedance resonator (a) $K = Z_2 / Z_1 < 1$ (b) $K = Z_2 / Z_1 > 1$ (c)Equivalent circuit model.....	14
Fig. 3.2. Resonant electrical length θ_t versus stepped percentage α with $K = 0.25, 0.5, 1, 2, 4$	16
Fig. 3.3. The relationship between f_s/f_0 and stepped percentage α with $K = 0.25, 0.5, 1, 2$, and 4	16
Fig. 3.4. Structure of a quarter-wavelength SIR	18
Fig. 3.5. SIR length versus impedance ratio	18
Fig. 3.6. Typical structure of the net-type resonator	19
Fig. 3.7. The procedure of resonator design	20
Fig. 4.1. Branch-line coupler with coupled resonators	23
Fig. 4.2. The coupling coefficient and external quality factor in a coupled resonator network (a) Coupling coefficient (b) external quality factor	23
Fig. 4.3. Equivalent coupled-resonator network of a branch-line coupler.....	24
Fig. 4.4. Schematic of lumped-element model	26
Fig. 4.5. Simulation result of lumped-element model	26
Fig. 4.6. Phase difference ($\angle S_{31} - \angle S_{21}$) of model	27
Fig. 4.7. Model constructed with magnetic coupling.....	28
Fig. 4.8. Simulation result of model with magnetic coupling.....	29
Fig. 4.9. Phase difference ($\angle S_{31} - \angle S_{21}$) of model with magnetic coupling	29

Fig. 4.10.	Layout of coupler design 1	31
Fig. 4.11.	Design features and characteristics for coupler design 1 in Fig. 4.10 (a) Coupling coefficient versus the distance between resonators (b) External quality factor versus the tapped line position of resonator	32
Fig. 4.12.	Photograph of fabricated coupler design 1	32
Fig. 4.13.	Simulation result of coupler design 1	33
Fig. 4.14.	Measurement result of coupler design 1	33
Fig. 4.15.	Measured and simulated performances of coupler design 1 ($ S_{11} $)	34
Fig. 4.16.	Measured and simulated performances of coupler design 1 ($ S_{21} $ & $ S_{31} $)	34
Fig. 4.17.	Measured and simulated performances of coupler design 1 ($ S_{41} $)	35
Fig. 4.18.	Measured and simulated performances of coupler design 1 ($\angle S_{31} - \angle S_{21}$)	35
Fig. 4.19.	The procedure of resonator design	36
Fig. 4.20.	Layout of coupler design 2	38
Fig. 4.21.	Design features and characteristics for coupler design 2 in Fig. 4.20 (a) Coupling coefficient versus the distance between resonators (b) External quality factor versus the tapped line position of resonator	38
Fig. 4.22.	Photograph of fabricated coupler design 2	40
Fig. 4.23.	Simulation result of coupler design 2	40
Fig. 4.24.	Measurement of coupler design 2	41
Fig. 4.25.	Measured and simulated performances of coupler design 2 ($ S_{11} $)	41
Fig. 4.26.	Measured and simulated performances of coupler design 2 ($ S_{21} $ & $ S_{31} $)	42
Fig. 4.27.	Measured and simulated performances of coupler design 2 ($ S_{41} $)	42
Fig. 4.28.	Measured and simulated performances of coupler design 2 ($\angle S_{31} - \angle S_{21}$)	43
Fig. 4.29.	Layout of coupler design 3	45
Fig. 4.30.	Design features and characteristics for coupler design 3 in Fig. 4.29 (a) Coupling coefficient versus the distance between resonators (b) External quality factor versus the tapped line position of resonator	45
Fig. 4.31.	Photograph of fabricated coupler design 3	46
Fig. 4.32.	Simulation result of coupler design 3	47
Fig. 4.33.	Measurement of coupler design 3	47
Fig. 4.34.	Measured and simulated performances of coupler design 3 ($ S_{11} $)	48
Fig. 4.35.	Measured and simulated performances of coupler design 3 ($ S_{21} $ & $ S_{31} $)	48
Fig. 4.36.	Measured and simulated performances of coupler design 3 ($ S_{41} $)	49

Fig. 4.37.	Measurement and simulation result of coupler design 3 ($\angle S_{31} - \angle S_{21}$)..	49
Fig. 4.38.	Layout of coupler design 4	51
Fig. 4.39.	Design features and characteristics for coupler design 4 in Fig. 4.38 (a) Coupling coefficient versus the distance between resonators (b) External quality factor versus the tapped line position of resonator	52
Fig. 4.40.	Photograph of fabricated coupler design 4	53
Fig. 4.41.	Simulation result of coupler design 4	53
Fig. 4.42.	Measurement of coupler design 4	54
Fig. 4.43.	Measured and simulated performances of coupler design 4 ($ S_{11} $)	54
Fig. 4.44.	Measured and simulated performances of coupler design 4 ($ S_{21} $ & $ S_{31} $)	55
Fig. 4.45.	Measured and simulated performances of coupler design 4 ($ S_{41} $)	55
Fig. 4.46.	Measurement and simulation results of coupler design 4 ($\angle S_{31} - \angle S_{21}$)	56
Fig. 4.47.	Layout of dual-band coupler.....	58
Fig. 4.48.	Design features and characteristics for dual-band coupler in Fig. 4.47 (a) Coupling coefficient versus the distance between resonators (b) External quality factor versus the tapped line position of resonator	58
Fig. 4.49.	Photograph of fabricated dual-band coupler	59
Fig. 4.50.	Simulation result of dual-band coupler	59
Fig. 4.51.	Measurement of dual-band coupler	60
Fig. 4.52.	Measured and simulated performances of dual-band coupler ($ S_{11} $).....	60
Fig. 4.53.	Measured and simulated performances of dual-band coupler ($ S_{21} $ & $ S_{31} $)	61
Fig. 4.54.	Measured and simulated performances of dual-band coupler ($ S_{41} $).....	61
Fig. 4.55.	Measured and simulated performances of dual-band coupler ($\angle S_{31} -$ $\angle S_{21}$)	62



Chapter 1

Introduction

1.1 Research Motivation

Directional coupler is an important component which can be used as power divider or combiner. It is widely used in microwave circuits and systems, such as balanced amplifier, balanced mixer, and antenna feeding network, etc.

In narrow-band applications, couplers and filters are designed separately and then cascaded. This approach occupies larger area and it is against the trend of miniaturization and integration. In this thesis, branch-line couplers composed of coupled resonators are presented. Traditional branch-line coupler is transformed into a coupled-resonator network. Using this approach, a bandpass branch-line coupler with compact size is achieved. In addition, a dual-band bandpass branch-line coupler is also presented.

1.2 Literature Survey

Branch-line coupler is one of the popular 90° couplers. Conventional branch-line coupler consists of 4 quarter-wavelength transmission lines. Its structure is simple and easy to design. However, it takes too much area because of the use of quarter-wavelength transmission lines. Many methods have been presented to reduce

circuit size. Folded transmission lines result in a compact structure [1]. Adopting of lumped elements also has been considered in [2-8]. This approach requires precise models for lumped elements. Another approach is replacing the traditional transmission lines with meta-materials [9], but the defective ground plane may limit its use.

Because of the popularity of multi-band applications such as cell phone and WiFi, branch-line couplers with dual-band characteristic are also desired. A dual-band branch-line coupler composed of right-hand/ left-hand transmission lines is presented in [10]. This approach requires models of lumped elements and has limited bandwidth. Another dual-band branch-line coupler utilizing quarter-wavelength open stub is proposed in [11]. However, these dual-band couplers do not have good bandpass characteristics. Additional filters are still needed in the system.

Recently, a new structure of branch-line coupler based on coupled resonators is introduced [12]. Using this technique, quarter-wavelength transmission lines are replaced with the couplings between resonators. Thus, a conventional branch-line coupler can be transformed into a coupled-resonator network (as shown in Fig. 1.1). The resultant branch-line coupler provides a bandpass response. Additionally, the size of branch-line coupler will reduce as the size of resonator shrinks. With miniaturized resonators, the circuit size will reduce 50% compared with conventional branch-line coupler.

This technique of transforming branch-line coupler into coupled-resonator network can be also extended to dual-band design. With stepped-impedance resonators, a dual-band branch-line coupler with bandpass response is achieved.

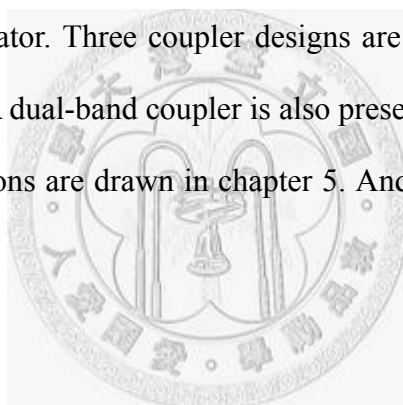
1.3 Organization of the Thesis

The research reported in this thesis is organized as follows. Chapter 2 presents the basic theory of couplings. The theory of electric/ magnetic couplings and external factor are introduced. The extraction of these parameters is also described.

In chapter 3, the analysis of stepped-impedance resonator (SIR) is presented. The characteristics of SIR and its design equations are given. The net-type resonator which is derived from SIR is also introduced. Then, a fork-like resonator is proposed.

Chapter 4 describes the concept and design procedure of the compact coupler composed of coupled resonators. The concept of this coupler is introduced and verified with circuit simulator. Three coupler designs are presented with simulations and experimental results. A dual-band coupler is also presented.

Finally, some conclusions are drawn in chapter 5. And the references are listed at the end of this thesis.



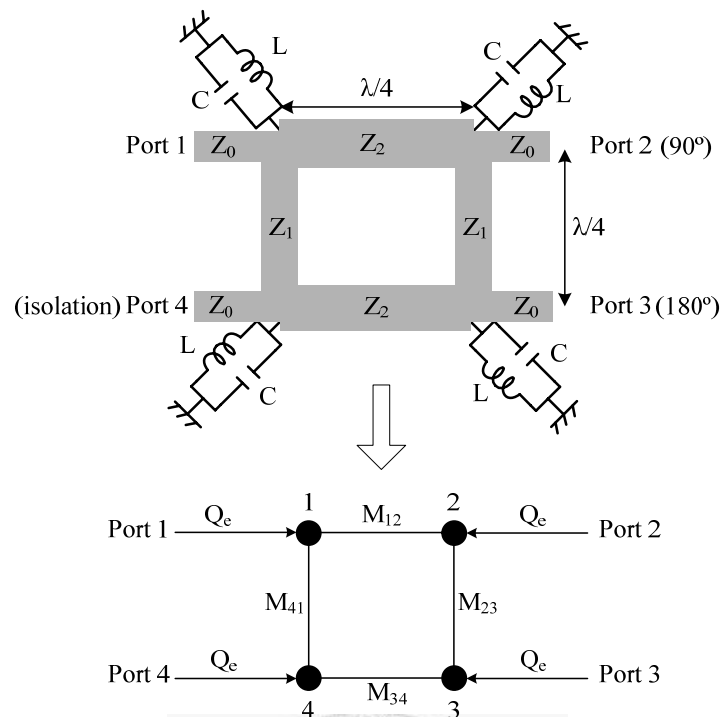
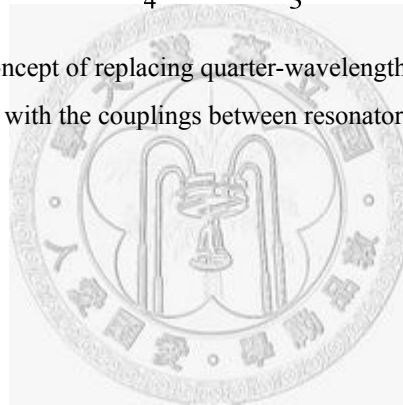


Fig. 1.1. The concept of replacing quarter-wavelength transmission lines with the couplings between resonators



Chapter 2

Basic Theory of Couplings

2.1 Basic Theory of Couplings

The coupled resonator is chosen as the basic building block in this thesis. It is commonly used in microwave filters. In order to establish the relationship between the designed parameters and the physical structure of coupled resonators, a technique which is originally applied to coupled-resonator filters [13] is introduced. This design method is based on coupling coefficients of intercoupled resonators and the external quality factors of the input and output resonators. The coupling coefficient of coupled resonators is defined as the ratio of coupled energy to stored energy of coupled resonators. In order to acquire the coupling coefficient, full-wave simulator is used to find some special frequencies related to the coupling of resonators. The method of extracting coupling coefficient and external quality factor is described as follows.

2.1.1 Electric Coupling

Fig. 2.1(a) illustrates the equivalent lumped-element circuit model of electrically coupled resonators. L and C are the self-inductance and self-capacitance, and C_m represents the mutual capacitance. The mutual capacitance shown in Fig. 2.1(a) can be replaced with a π network as shown in Fig. 2.1(b). Thus, the electric coupling between resonators can be represented as an admittance inverter $J = \omega C_m$.

Then, this symmetric circuit is analyzed with even mode and odd mode,

respectively. In even mode, the symmetry plane $T - T'$ is replaced with an electric wall, the circuit resonates at

$$f_e = \frac{1}{2\pi\sqrt{L(C + C_m)}}. \quad (2.1)$$

Similarly, the symmetry plane is replaced with a magnetic wall in odd mode. The resultant resonant frequency is

$$f_m = \frac{1}{2\pi\sqrt{L(C - C_m)}}. \quad (2.2)$$

The even-mode resonant frequency is lower than that of an uncoupled single resonator, and the odd-mode resonant frequency is higher than that of an uncoupled resonator. From equations (2.1) and (2.2), the electric coupling coefficient M_E can be found as

$$M_E = \frac{C_m}{C} = \frac{f_m^2 - f_e^2}{f_m^2 + f_e^2}. \quad (2.3)$$

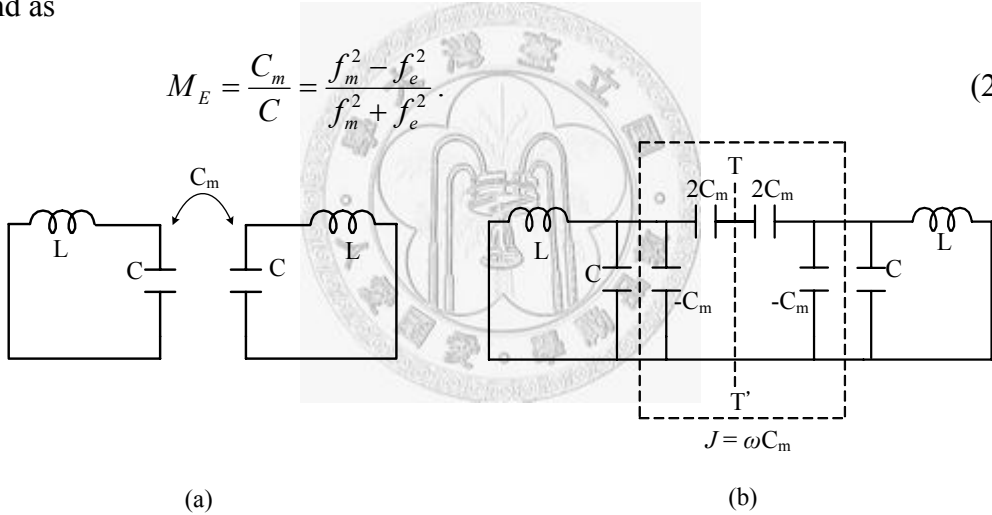


Fig. 2.1. (a) Coupled resonator circuit with electric coupling (b) An alternative form of the equivalent circuit

2.1.2 Magnetic Coupling

Fig. 2.2(a) illustrates the equivalent lumped-element circuit model for magnetically coupled resonators. L and C are the self-inductance and self-capacitance, and L_m represents the mutual inductance. The mutual inductance can be replaced with a T network as shown in Fig. 2.2(b). Thus, the magnetic coupling between resonators can be represented as an admittance inverter $K = \omega L_m$.

The even/odd-mode analysis is also applied here. In even mode, the symmetry plane $T - T'$ is replaced with an electric wall, the circuit resonates at

$$f_e = \frac{1}{2\pi\sqrt{(L - L_m)C}}. \quad (2.4)$$

Similarly, the symmetry plane is replaced with a magnetic wall in odd mode. The resultant resonant frequency is

$$f_m = \frac{1}{2\pi\sqrt{(L + L_m)C}}. \quad (2.5)$$

The even-mode resonant frequency is higher than that of an uncoupled single resonator, and the odd-mode resonant frequency is lower than that of an uncoupled resonator. From equations (2.4) and (2.5), the electric coupling coefficient M_M can be found as

$$M_M = \frac{L_m}{L} = \frac{f_e^2 - f_m^2}{f_e^2 + f_m^2}. \quad (2.6)$$

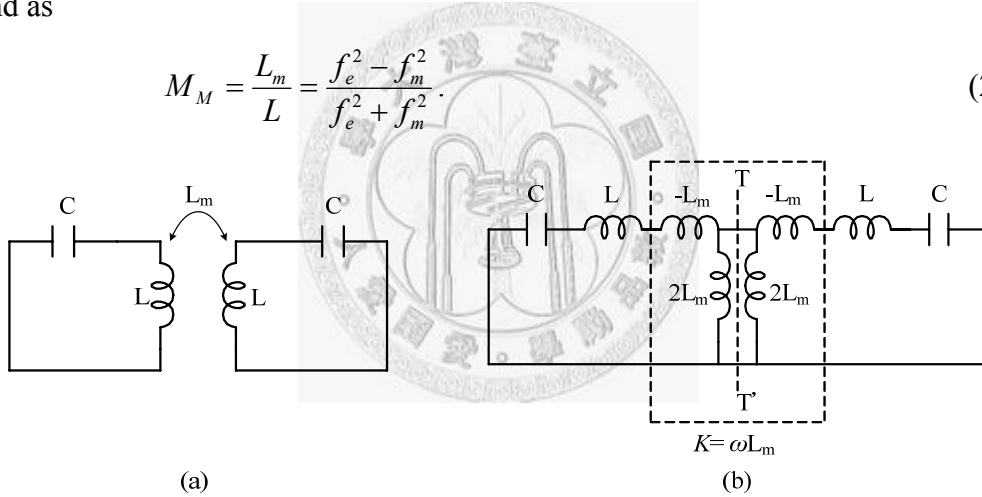


Fig. 2.2. (a) Coupled resonator circuit with magnetic coupling (b) An alternative form of the equivalent circuit

2.1.3 Mixed Coupling

Fig. 2.3 shows the equivalent circuit model of coupled resonators with both electric and magnetic couplings. The impedance inverter $K = \omega L_m$ and the admittance inverter $J = \omega C_m$ in Fig. 2.3 represent the magnetic and electric couplings, respectively.

Using the same procedure applied above, replacing the symmetry plane $T - T'$

with electric wall results in a resonant frequency

$$f_e = \frac{1}{2\pi\sqrt{(L-L_m)(C-C_m)}} \quad (2.7)$$

Replacing the symmetry plane $T-T'$ with magnetic wall results in another resonant frequency

$$f_m = \frac{1}{2\pi\sqrt{(L+L_m)(C+C_m)}} \quad (2.8)$$

From equations (2.7) and (2.8), the coupling coefficient of mixed coupling M_X can be found as

$$M_X = \frac{CL_m + LC_m}{LC + L_m C_m} = \frac{f_e^2 - f_m^2}{f_e^2 + f_m^2} \quad (2.9)$$

Assuming that $L_m C_m \ll LC$, equation (2.9) becomes

$$M_X \approx \frac{L_m}{L} + \frac{C_m}{C} = M_M + M_E \quad (2.10)$$

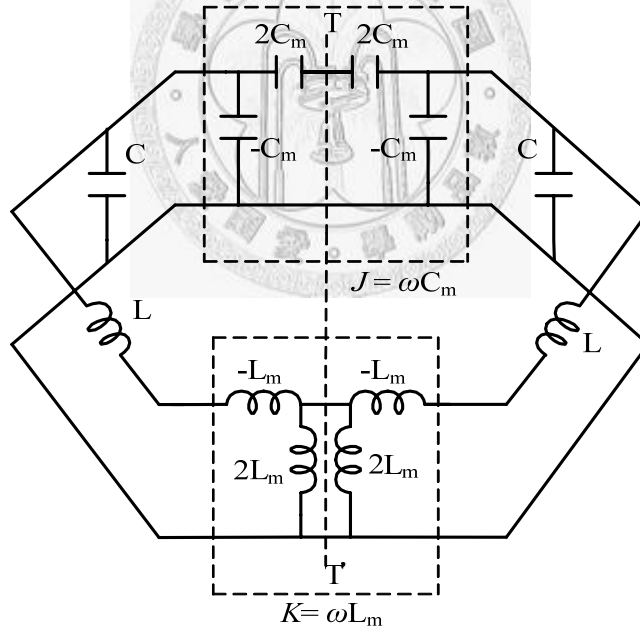


Fig. 2.3. An equivalent lumped-element circuit with both electric and magnetic couplings

2.1.4 External Quality Factor

Fig. 2.4(a) shows the equivalent circuit model for extracting the external quality factor. G is the external conductance attached to the lossless LC resonator. From this model, S_{11} of the excitation port can be represented as

$$S_{11} = \frac{G - Y_{in}}{G + Y_{in}} = \frac{1 - Y_{in}/G}{1 + Y_{in}/G}, \quad (2.11)$$

where Y_{in} is the input admittance of the resonator

$$Y_{in} = j\omega C + \frac{1}{j\omega L} = j\omega C \left(\frac{\omega}{\omega_0} - \frac{\omega_0}{\omega} \right). \quad (2.12)$$

In the equation above, $\omega_0 = 1/\sqrt{LC}$ is the resonant frequency. Near resonant frequency, i.e., $\omega = \omega_0 + \Delta\omega$, the approximation $(\omega^2 - \omega_0^2)/\omega \approx 2\Delta\omega$ is valid. Then,

(2.12) can be written as

$$Y_{in} = j\omega C \cdot \frac{2\Delta\omega}{\omega_0}. \quad (2.13)$$

The equation (2.11) can be written as follows via applying (2.13) and $Q_e = \omega_0 C/G$.

$$S_{11} = \frac{1 - jQ_e \cdot (2\Delta\omega/\omega_0)}{1 + jQ_e \cdot (2\Delta\omega/\omega_0)}. \quad (2.14)$$

If the resonator is lossless, the magnitude of S_{11} in (2.14) is always equal to 1 because the parallel resonator works as an open circuit near resonant frequency. On the contrary, the phase response of S_{11} changes against frequency (as shown in Fig. 2.4(b)). When the phase equals to $\pm 90^\circ$, the corresponding value of $\Delta\omega$ is found as

$$2Q_e \cdot \frac{\Delta\omega_{\mp 90^\circ}}{\omega_0} = \mp 1. \quad (2.15)$$

Therefore, the bandwidth between the $\pm 90^\circ$ points is

$$\Delta\omega_{\mp 90^\circ} = \Delta\omega_+ - \Delta\omega_- = \frac{\omega_0}{Q_e}. \quad (2.16)$$

The external quality factor can then be found from the relation

$$Q_e = \frac{\omega_0}{\Delta\omega_{\pm 90^\circ}}. \quad (2.17)$$

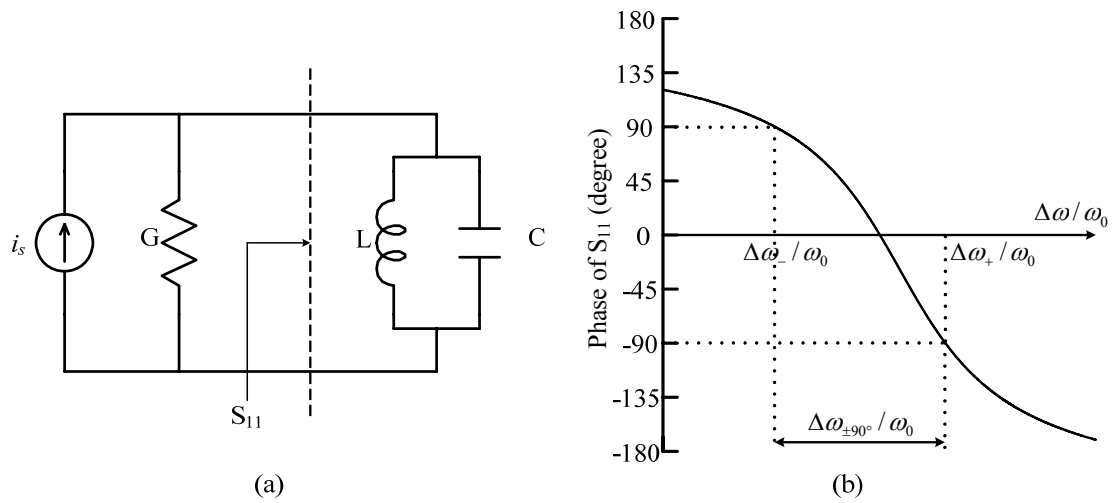


Fig. 2.4. (a) Equivalent circuit of the I/O resonator with a single load (b) Phase response of S_{11}

2.2 Impedance and Admittance Inverters

Impedance (K) and admittance (J) inverters are commonly used building blocks in filter design, especially for narrow-band bandpass or bandstop filters. The conceptual operation of impedance and admittance inverters and some implementations of the inverters are illustrated in Fig. 2.5, which is adopted from [14]. As shown in Fig. 2.5(b), a quarter-wavelength transmission line is equivalent to a J or K inverter. Besides, J or K inverters can also be implemented with other kinds of circuits such as capacitor network. Some examples are shown in Fig. 2.5(c)(d).

Inverters constructed with capacitor or inductor networks are very useful for modeling the coupled resonators. In the next chapter, coupled resonators and J inverters in Fig. 2.5(d) will be used to construct branch-line couplers.

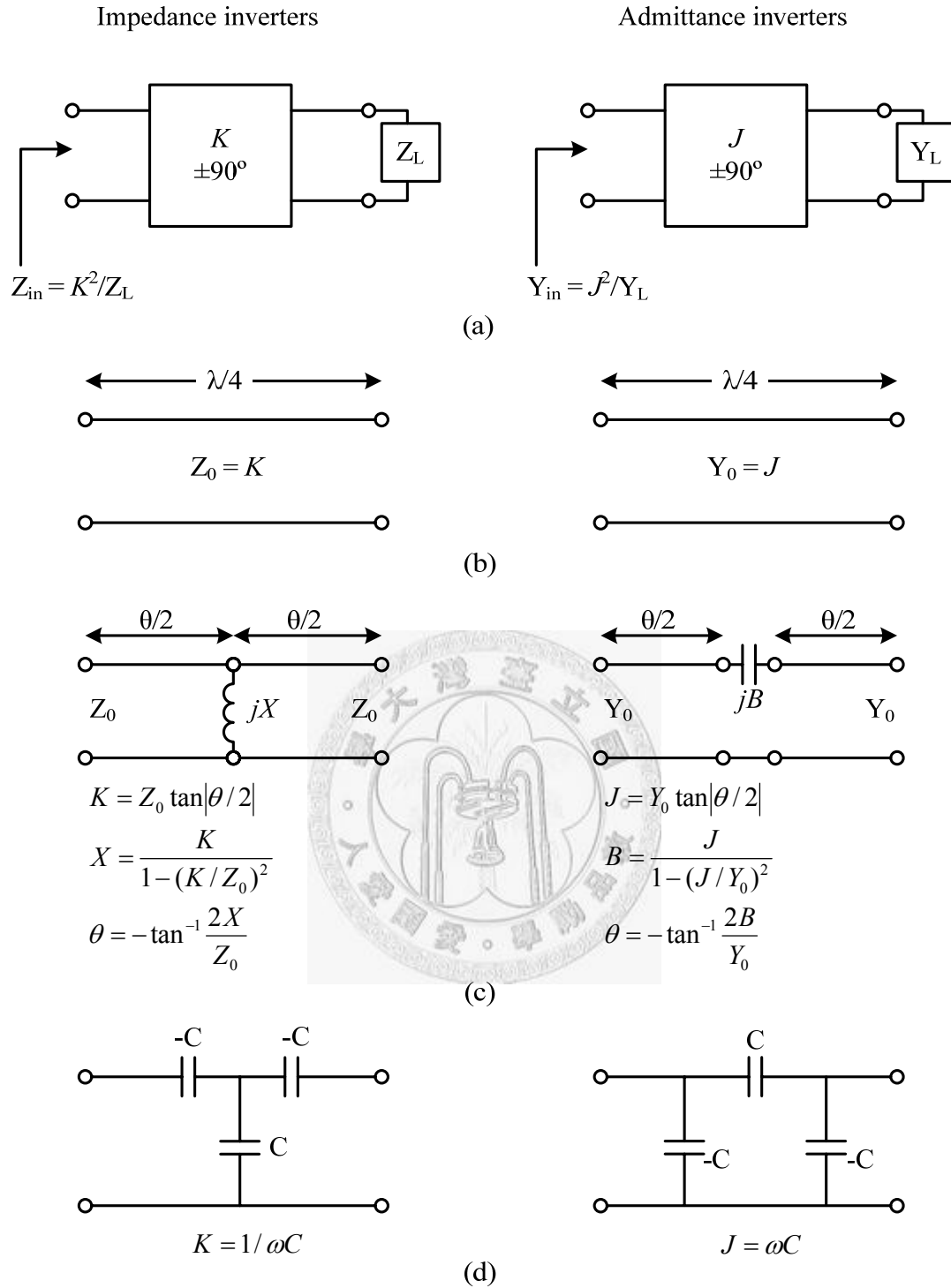


Fig. 2.5. Impedance and admittance inverters (a) Operation of impedance and admittance inverters (b) Implementation as quarter-wave transformers (c) Implementation using transmission lines and reactive elements (d) Implementation using capacitor networks



Chapter 3

Analysis of Stepped-Impedance

Resonators

Stepped-impedance resonator is one of the most frequently used resonators because it not only reduces the resonator size but also controls all of the resonant frequencies [15, 16]. In this chapter, complete design equations for SIRs and its characteristics will be presented.

3.1 Resonant Conditions

A half-wavelength SIR is a symmetrical structure which has two different characteristic impedances, Z_1 and Z_2 , or admittances Y_1 and Y_2 , with the corresponding electrical lengths θ_1 and θ_2 as shown in Fig. 3.1. K is the impedance ratio defined as

$$K = \frac{Y_1}{Y_2} = \frac{Z_2}{Z_1}. \quad (3.1)$$

The typical structures of SIR can be divided into two categories, $K < 1$ and $K > 1$. Fig. 3.1(c) shows the equivalent model of a SIR. When the SIR operates in its odd modes, i.e., the symmetry plane $T-T'$ is replaced by a short circuit, the impedances Z_A^o and Z_B^o as illustrated in Fig. 3.1(c) can be found to be

$$Z_A^o = jZ_1 \cdot \tan \theta_1$$

and

$$Z_B^o = -jZ_2 \cdot \cot \theta_2. \quad (3.2)$$

When the SIR operates in its even modes, the symmetry plane $T-T'$ is replaced with an open circuit. Then, their impedances Z_A^e and Z_B^e can be found to be

$$Z_A^e = -jZ_1 \cdot \cot \theta_1$$

and

$$Z_B^e = -jZ_2 \cdot \cot \theta_2. \quad (3.3)$$

Therefore, the resonant conditions of SIRs can be derived by enforcing the conditions of $Z_A^o = (Z_B^o)^*$ and $Z_A^e = (Z_B^e)^*$. The equations can be written as follows.

$$K \cdot \cot \theta_2 = \tan \theta_1 \quad (3.4)$$

and

$$K \cdot \cot \theta_2 = -\cot \theta_1, \quad (3.5)$$

where (3.4) corresponds to the odd-mode resonance and (3.5) corresponds to the even-mode resonance.

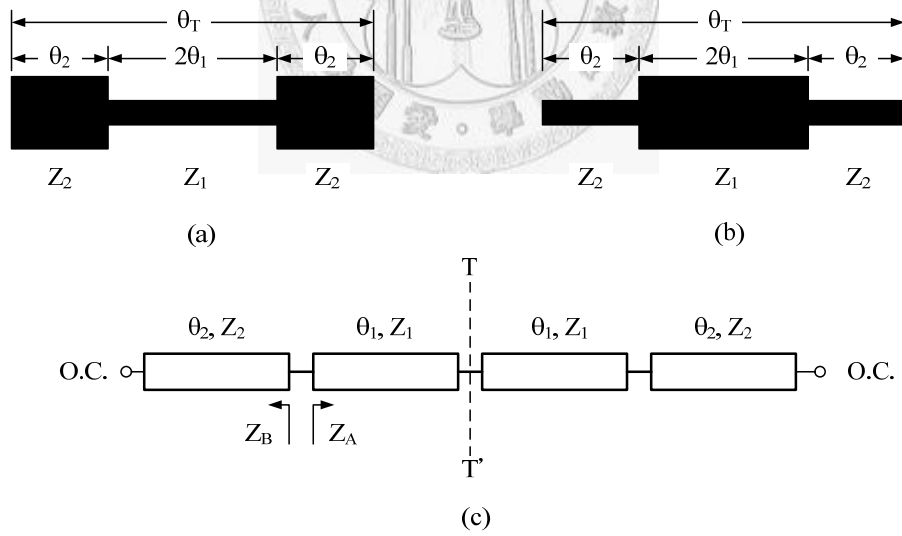


Fig. 3.1. Structure of the stepped-impedance resonator (a) $K = Z_2 / Z_1 < 1$ (b) $K = Z_2 / Z_1 > 1$
(c) Equivalent circuit model

3.2 Characteristics of SIRs

In the following analysis, the propagation constants of the transmission line sections are assumed weakly dependent on the width and the junction effects are neglected. Therefore, the electrical lengths in (3.4) and (3.5) are proportional to the physical lengths. The stepped percentage α is defined as the ratio of the electrical length of transmission line 2 to that of the whole transmission line, i.e.,

$$2\theta_2 = \alpha \cdot \theta_T, \quad (3.6)$$

where $\theta_T = 2(\theta_1 + \theta_2)$ is the total electrical length of the SIR.

Substituting (3.6) into (3.4) and (3.5) yields

$$K \cdot \cot\left[\frac{1}{2}\alpha \cdot \theta_T\right] = \tan\left[\frac{1}{2}(1-\alpha) \cdot \theta_T\right], \quad (3.7)$$

and

$$K \cdot \cot\left[\frac{1}{2}\alpha \cdot \theta_T\right] = -\cot\left[\frac{1}{2}(1-\alpha) \cdot \theta_T\right], \quad (3.8)$$

There are numerous solutions for θ_T depending on the choice of α and K . The fundamental resonance and higher-order resonances of SIR can be controlled by choosing α and K appropriately. The relationship between the resonant electrical length θ_T and α with $K = 0.25, 0.5, 1, 2,$ and 4 are shown in Fig. 3.2, which is obtained by solving these two equations.

In the non-stepped case, $K = 1$ and $\alpha = 0$ or 1 , the resonant electrical length θ_T is $n\pi$, i.e., the n th resonance occurs when the total length is equal to n times of the half wavelength. Thus, the ratio of the first spurious frequency f_{s1} to the fundamental frequency f_0 is 2. In cases of $K < 1$, this ratio is larger than 2, and it is smaller than 2 if $K > 1$. The relationship between this ratio and stepped percentage α with $K = 0.25, 0.5, 1, 2$ is shown in Fig. 3.3. The deviation of the ratio is more significant for larger α .

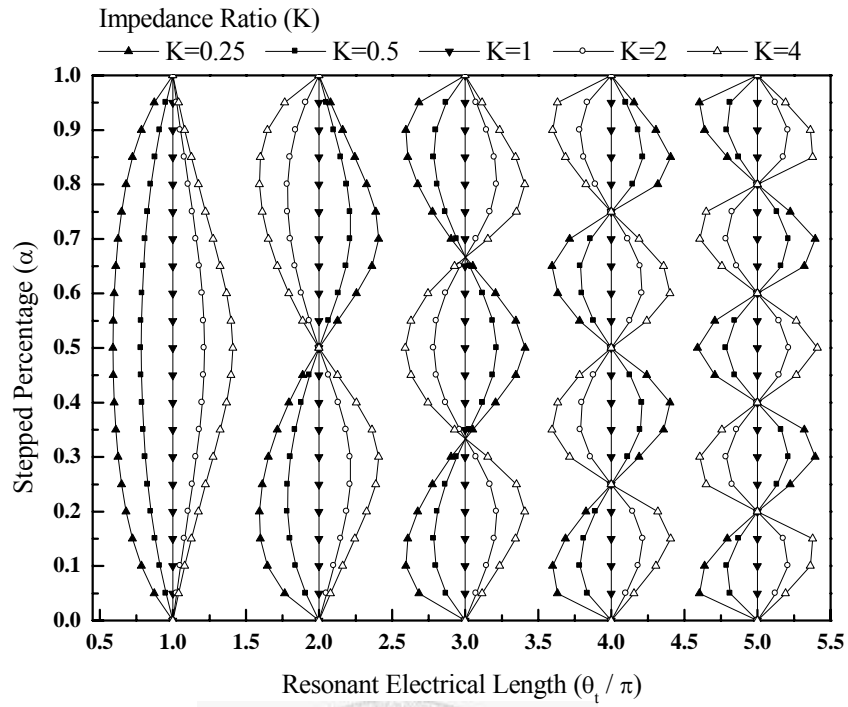


Fig. 3.2. Resonant electrical length θ_t versus stepped percentage α with $K = 0.25, 0.5, 1, 2, 4$

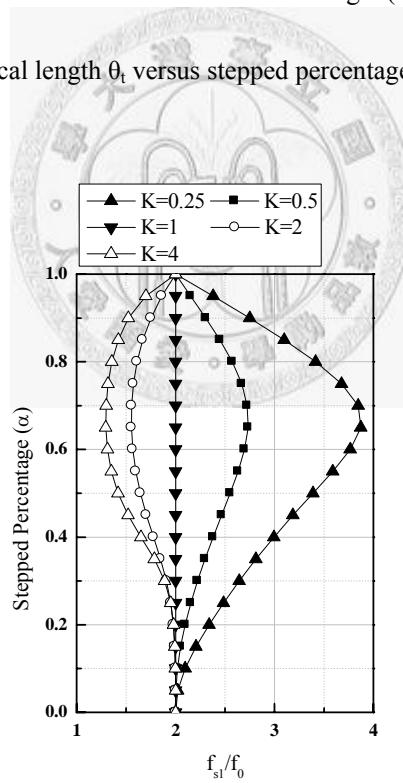


Fig. 3.3. The relationship between f_{s1}/f_0 and stepped percentage α with $K = 0.25, 0.5, 1, 2, 4$

3.3 Quarter-Wavelength SIRs

Fig. 3.4 shows the structure of a typical shorted quarter-wavelength SIR. This kind of resonator is composed of two sections of transmission line with different characteristic impedance. The characteristic impedances and the electrical lengths of these two transmission lines are Z_1 , Z_2 , θ_1 , and θ_2 , respectively. Its resonance condition is the same as the odd-mode resonances of half-wavelength SIRs, as shown in (3.4). Similarly, the fundamental resonance and higher-order resonances can be controlled by the impedance ratio K and stepped-percentage α . When the impedance ratio of the quarter-wavelength SIR is much smaller than unity, the ratio of the first spurious resonant frequency f_{s1} to the fundamental resonant frequency f_0 becomes very large. This phenomenon results in a very wide stopband.

In order to evaluate the minimum electrical length of quarter-wavelength SIR, the equation followed is used.

$$\frac{d}{d\theta_2} [\tan(\theta_1 + \theta_2)] = 0, \quad (3.9)$$

Since

$$\tan(\theta_1 + \theta_2) = \frac{\tan \theta_1 + \tan \theta_2}{1 - \tan \theta_1 \cdot \tan \theta_2} = \frac{K \cot \theta_2 + \tan \theta_2}{1 - K}, \quad (3.10)$$

the result of the minimum electrical length is as follows.

$$\theta_T = \theta_1 + \theta_2 = 2 \cdot \tan^{-1} \sqrt{K}, \quad (3.11)$$

where

$$\theta_1 = \theta_2. \quad (3.12)$$

From the solution derived above, the resonator length of a quarter-wavelength SIR can be reduced. Fig. 3.5 plots the impedance ratio of a quarter-wavelength SIR with respect to the SIR length θ_T , when $\theta_1 = \theta_2$.

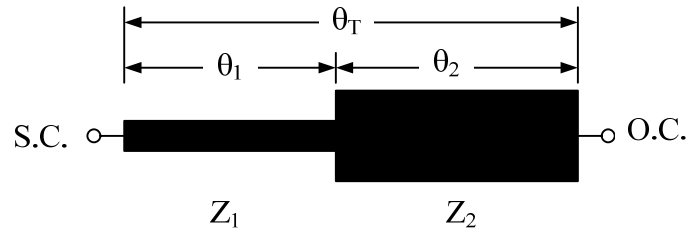


Fig. 3.4. Structure of a quarter-wavelength SIR

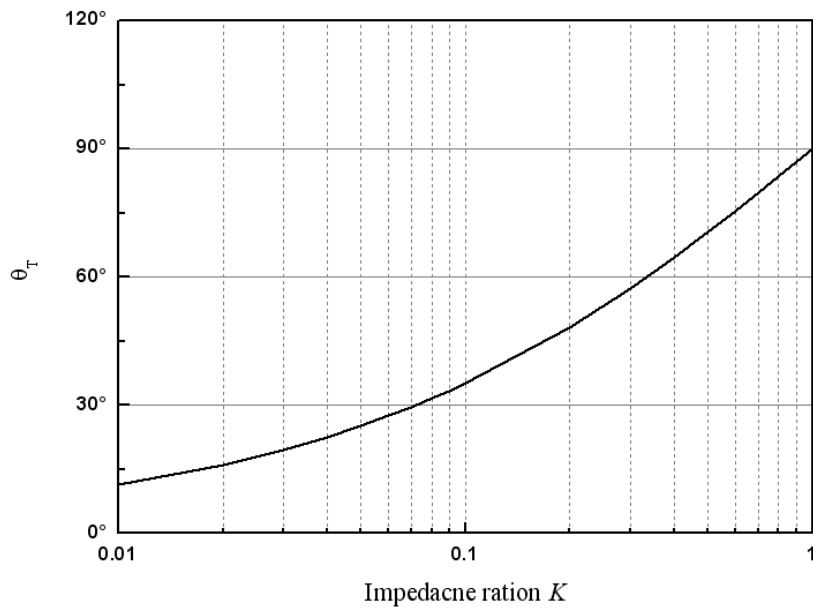


Fig. 3.5. SIR length versus impedance ratio

3.4 Net-Type Resonators

The net-type resonator is a variation of quarter-wavelength SIR [17, 18]. The low-impedance section is replaced by parallel-connected high-impedance transmission lines. The typical structure of the net-type resonator is illustrated in Fig. 3.6 in which N denotes the number of parallel-connected open-end high-impedance transmission lines. When the impedance of all transmission-line sections are the same, it is equivalent to a SIR with an impedance ratio of $N : 1$.

Similar to the quarter-wavelength SIR, the resonant condition of the net-type resonator can be written as

$$\frac{1}{N} \cot \theta_2 = \tan \theta_1, \quad (3.13)$$

where θ_1 and θ_2 are the electrical lengths of the short-ended and open-ended transmission line sections of the net-type resonator, respectively. As mentioned in the previous section, the minimum electrical length of a net-type SIR is

$$\theta_T = \theta_1 + \theta_2 = 2 \cdot \tan^{-1} \left(\frac{1}{\sqrt{N}} \right), \quad (3.14)$$

where $\theta_1 = \theta_2$.

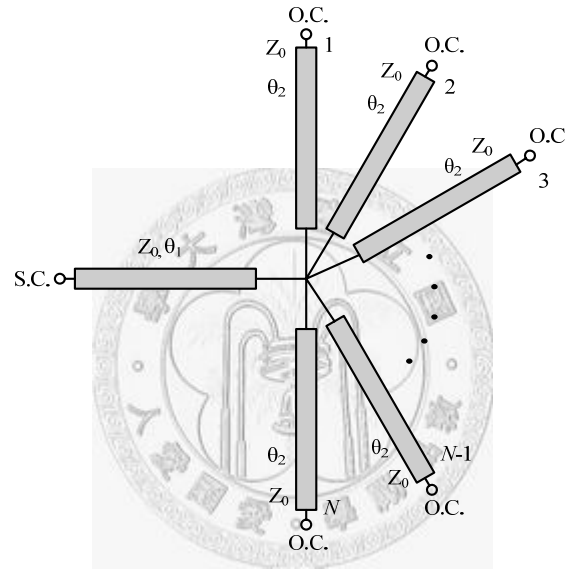


Fig. 3.6. Typical structure of the net-type resonator

3.5 Designed Resonators

Because the design target is miniaturized coupler, smaller resonators are desired. From the discussions above, if the impedance ratio K is smaller than 1, the length of resonators will reduce. But there are some restrictions in practical design. In microstrip structure, wider strip width results in not only lower characteristic impedance but also weaker coupling. This property restricts the bandwidth of the circuit.

In order to overcome this drawback, the concept of net-type resonator is adopted.

Fig. 3.7 shows the procedure of resonator design. The low-impedance section of SIR is replaced with parallel-connected high-impedance transmission lines. Thus, a fork-like resonator comes into being. Although the structure is slightly different from the original net-type resonator, the design equations are still available.

This fork-like resonator provides stronger couplings with adjacent resonators and remains small size at the same time. It is suitable for the coupler design described in the next chapter.

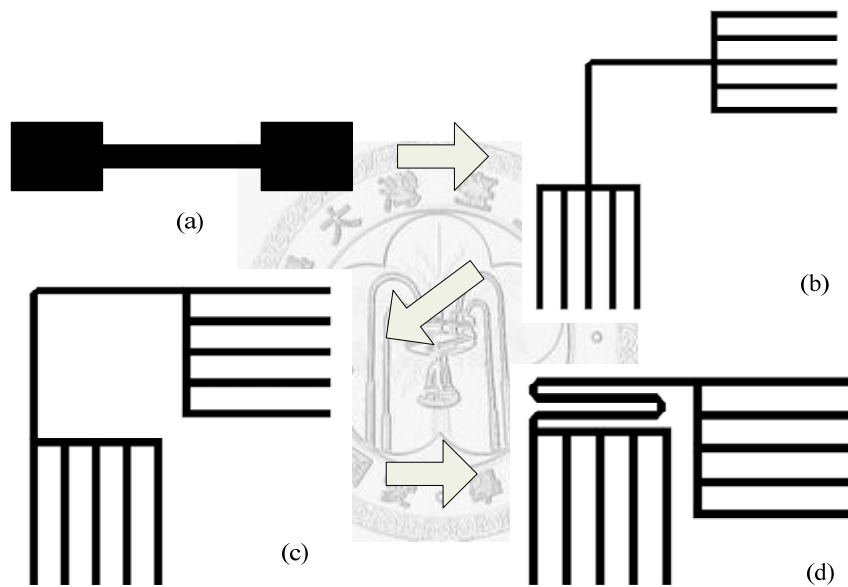


Fig. 3.7. The procedure of resonator design

Chapter 4

Design of Compact Branch-Line Couplers with Coupled Resonators

Branch-line coupler consists of four quarter-wavelength transmission lines. This structure is simple and easily fabricated, but occupies too much area. In the past, many structures such as capacitive loading, lumped elements, left-hand/right-hand materials are proposed to reduce its size.

Recently, a structure based on coupled resonators is proposed [12]. This technique replaces quarter-wavelength transformer with couplings between resonators. Therefore, the size of coupler reduces as the resonator becomes smaller. Besides, the branch-line coupler designed with this approach provides bandpass characteristics. Thus, the coupler and filters are combined together and the circuit size is reduced. This technique is suitable for narrow-band applications.

Additionally, a dual-band branch-line coupler based on this approach is also proposed. With stepped-impedance resonators, the dual-band branch-line coupler with bandpass characteristics is presented.

In the beginning of this chapter, the design method is presented. In order to observe the frequency responses, the models utilizing electric coupling and magnetic coupling are also presented, respectively. Followed are four designs of branch-line coupler and a dual-band branch-line coupler.

4.1 Equivalent Circuit of Branch-Line Coupler

Fig. 4.1 shows the concept of this coupler design method. According to the definition in [14], port 1, 2, 3, 4 are input, 90°, 180°, and isolation, respectively. It consists of a conventional branch-line coupler with four shunted resonators at each port. These resonators resonate at the center frequency of the coupler, i.e.,

$$\omega_0^2 = \frac{1}{LC}. \quad (4.1)$$

When the resonators resonate, it looks like an open circuit and does not affect the original function of the coupler.

Then, the quarter-wavelength transmission lines are replaced with the couplings between the resonators according to the theory of J/K inverters presented in section 3.2. Fig. 4.2 shows the relationship between the impedance of quarter-wavelength transmission line and coupling coefficients/external quality factor. Through this relationship, a branch-line coupler can be transformed into a coupled-resonator network as shown in Fig. 4.3, which is commonly used in microwave filter design. And the design formulas are listed below.

$$M_{12} = M_{34} = \frac{1}{\omega_0 CZ_2} \quad (4.2)$$

$$M_{23} = M_{41} = \frac{1}{\omega_0 CZ_1} \quad (4.3)$$

$$Q_e = \omega_0 CZ_0 \quad (4.4)$$

For a 3-dB branch-line coupler, $Z_0 = Z_1 = \sqrt{2}Z_2$. These design equations can be rewritten as

$$M_{12} = M_{34} = \frac{\sqrt{2}}{\omega_0 CZ_0} = \frac{\sqrt{2}}{Q_e} \quad (4.5)$$

and

$$M_{23} = M_{41} = \frac{1}{\omega_0 CZ_0} = \frac{1}{Q_e} \quad (4.6)$$

Once we choose the external quality factor, other parameters are decided. Theoretically, smaller external quality factor and larger coupling coefficient result in larger bandwidth.

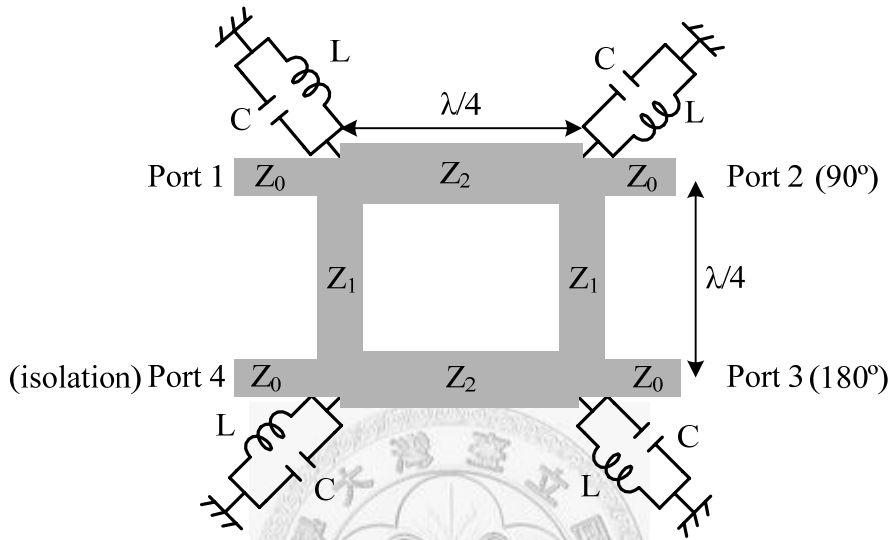


Fig. 4.1. Branch-line coupler with coupled resonators

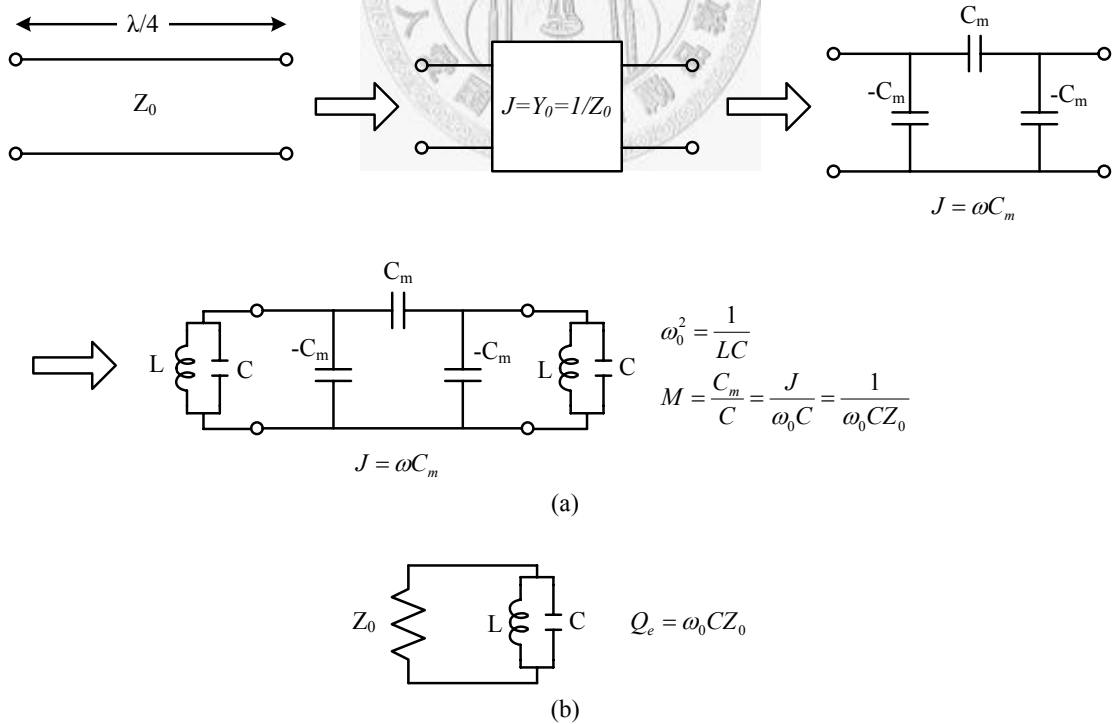


Fig. 4.2. The coupling coefficient and external quality factor in a coupled resonator network
 (a) Coupling coefficient (b) external quality factor

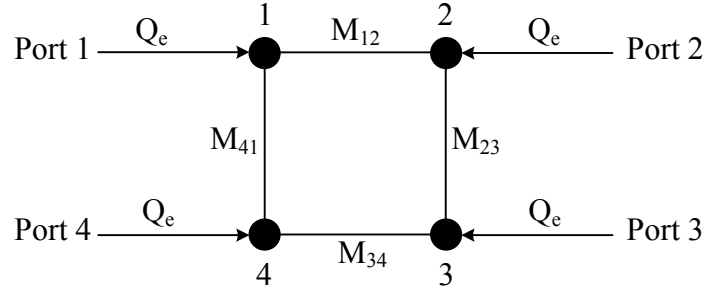


Fig. 4.3. Equivalent coupled-resonator network of a branch-line coupler

In order to observe the frequency response and verify the feasibility of this equivalent coupled-resonator network, we use lumped inductors and capacitors to construct a model in circuit simulator Microwave Office. The schematic is shown in Fig. 4.4. The half-wavelength resonator is modeled as a parallel LC resonator. The couplings and external quality factors are modeled as capacitor networks and transformers respectively.

For an open-circuited half-wavelength resonator, its capacitance is

$$C = \frac{\pi}{2\omega_0 Z_0}, \quad (4.7)$$

and its inductance is

$$L = \frac{1}{\omega_0^2 C}, \quad (4.8)$$

where ω_0 is the resonant frequency as well as the central frequency of designed branch-line coupler.

Other parameters are obtained as follows.

$$C_{m1} = M_{12}C = M_{12} \times \frac{\pi}{2\omega_0 Z_0}, \quad (4.9)$$

$$C_{m2} = M_{23}C = M_{23} \times \frac{\pi}{2\omega_0 Z_0}, \quad (4.10)$$

and

$$n = \sqrt{\frac{Q_e}{\omega_0 C Z_0}}. \quad (4.11)$$

The central frequency is set as 2GHz for demonstration. The coupling coefficients and external quality factor are chosen as

$$Q_e = 10,$$

$$M_{12} = M_{34} = \frac{\sqrt{2}}{Q_e} = 0.1414,$$

$$M_{23} = M_{41} = \frac{1}{Q_e} = 0.1.$$

The values of lumped elements are listed as follows.

$$Z_0 = 50\Omega$$

$$C = \frac{\pi}{2\omega_0 Z_0} = 2.5\text{ pF}$$

$$L = \frac{1}{\omega_0^2 C} = 2.533\text{ nH}$$

$$C_{m1} = M_{12}C = 0.3535\text{ pF}$$

$$C_{m2} = M_{23}C = 0.25\text{ pF}$$

$$n = \sqrt{\frac{Q_e}{\omega_0 C Z_0}} = 2.5231$$

The simulation result of the model is shown in Fig. 4.5 and Fig. 4.6. It can be observed in Fig. 4.5 that there are some ripples in the passband. However, this circuit still has good off-band rejection. In practical design, $|S_{21}|$ will be slightly increased in order to increase bandwidth. Fig. 4.6 shows the phase difference of through port and coupled port ($\angle S_{31} - \angle S_{21}$) in lumped-element model. There will be 90° phase difference at central frequency.

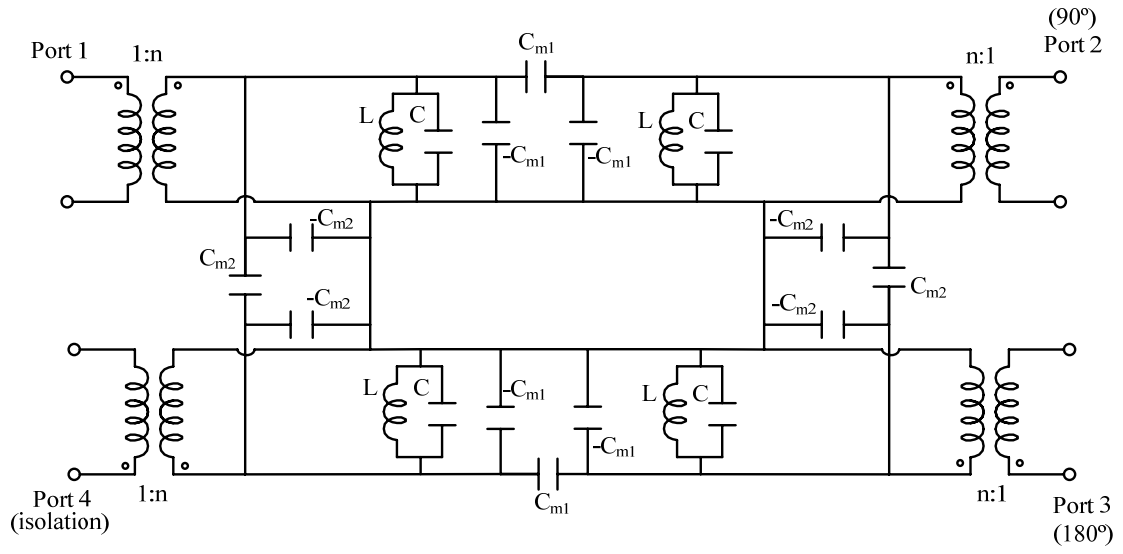


Fig. 4.4. Schematic of lumped-element model

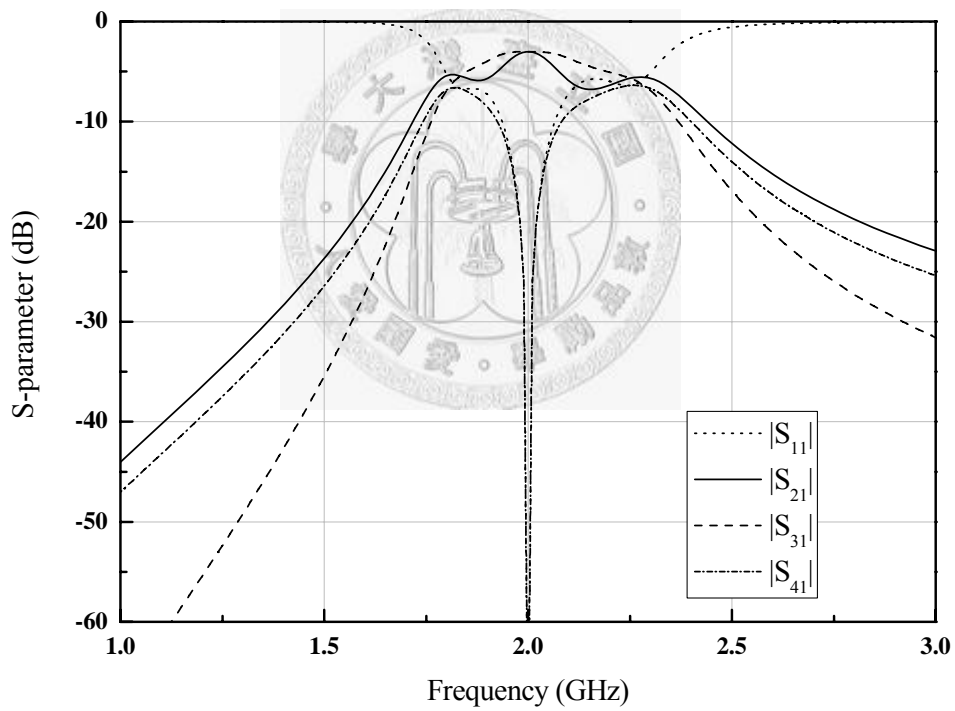


Fig. 4.5. Simulation result of lumped-element model

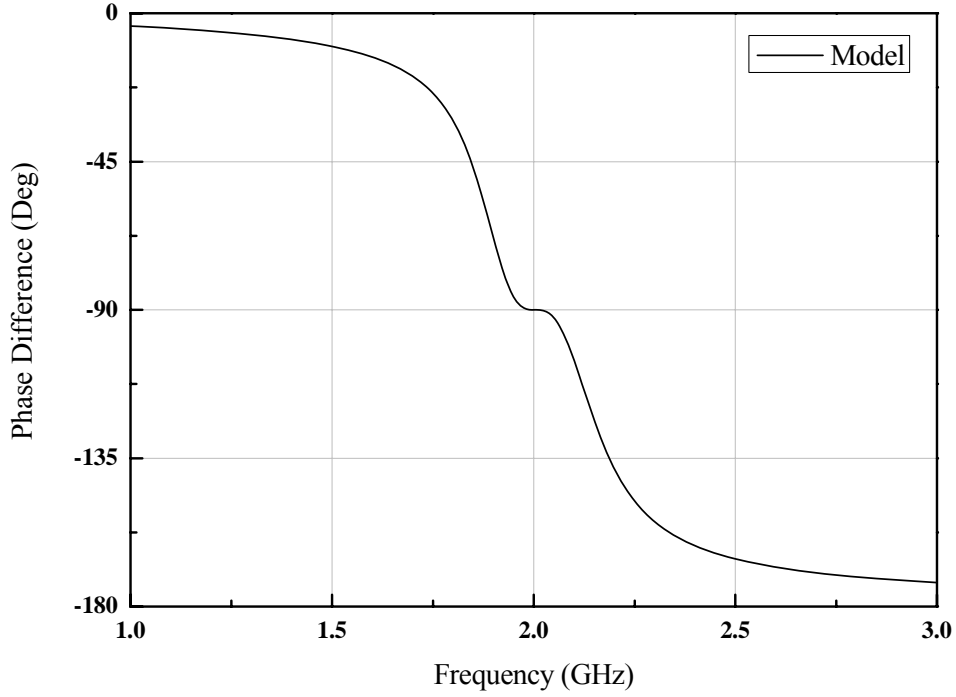


Fig. 4.6. Phase difference ($\angle S_{31} - \angle S_{21}$) of model

Although the model demonstrated above utilizes electric coupling, magnetic coupling results in similar response. Fig. 4.7 shows the model constructed with magnetic coupling. Similarly, the center frequency of this model is also set at 2GHz. The parameters chosen are listed below, which are the same as those of the model above.

$$Q_e = 10,$$

$$M_{12} = M_{34} = \frac{\sqrt{2}}{Q_e} = 0.1414,$$

$$M_{23} = M_{41} = \frac{1}{Q_e} = 0.1.$$

The values of lumped elements are listed as follows.

$$Z_0 = 50\Omega$$

$$C = \frac{\pi}{2\omega_0 Z_0} = 2.5 pF$$

$$L = \frac{1}{\omega_0^2 C} = 2.533nH$$

$$L_{m1} = M_{12}L = 0.358nH$$

$$L_{m2} = M_{23}L = 0.253nH$$

$$n = \sqrt{\frac{Q_e}{\omega_0 CZ_0}} = 2.5231$$

The simulation results are shown in Fig. 4.8 and Fig. 4.9. Similar to the results above, this model has some ripples and good off-band rejection. Compared with the model with electric coupling, the frequency response of this model is more asymmetric. Fig. 4.9 shows the phase difference between through port and coupled port ($\angle S_{31} - \angle S_{21}$). There is a 90° phase difference at center frequency, too.

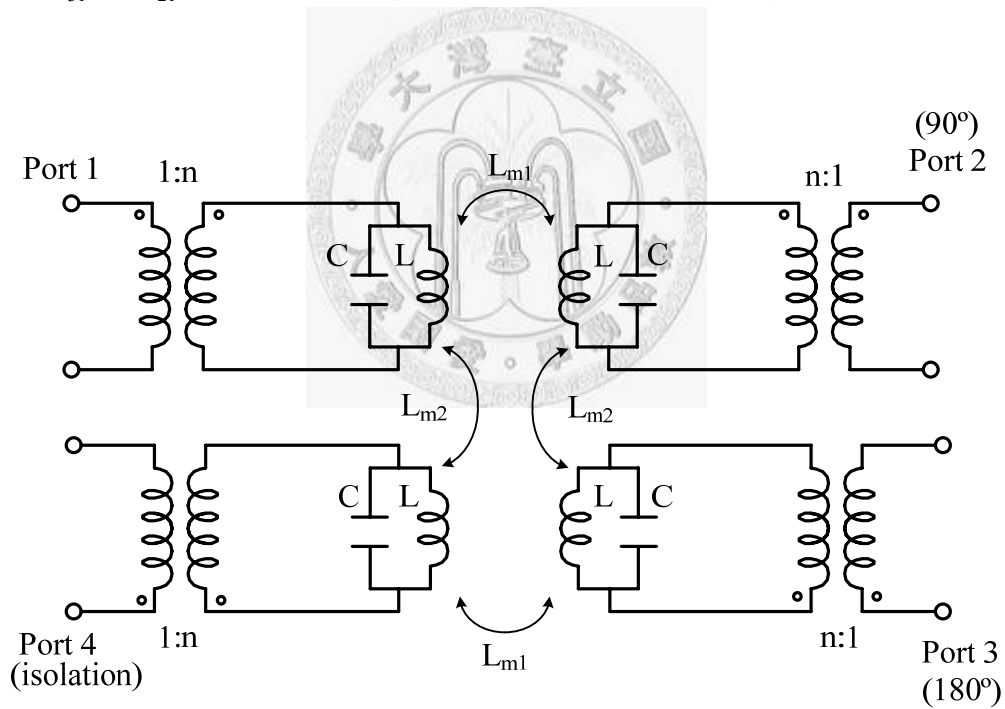


Fig. 4.7. Model constructed with magnetic coupling

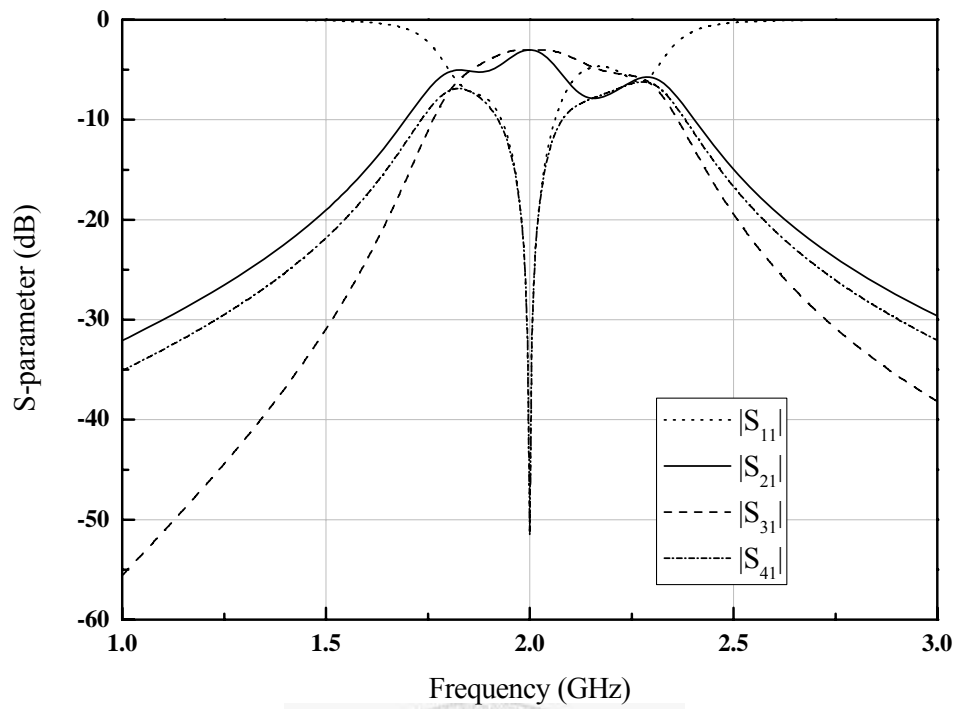


Fig. 4.8. Simulation result of model with magnetic coupling

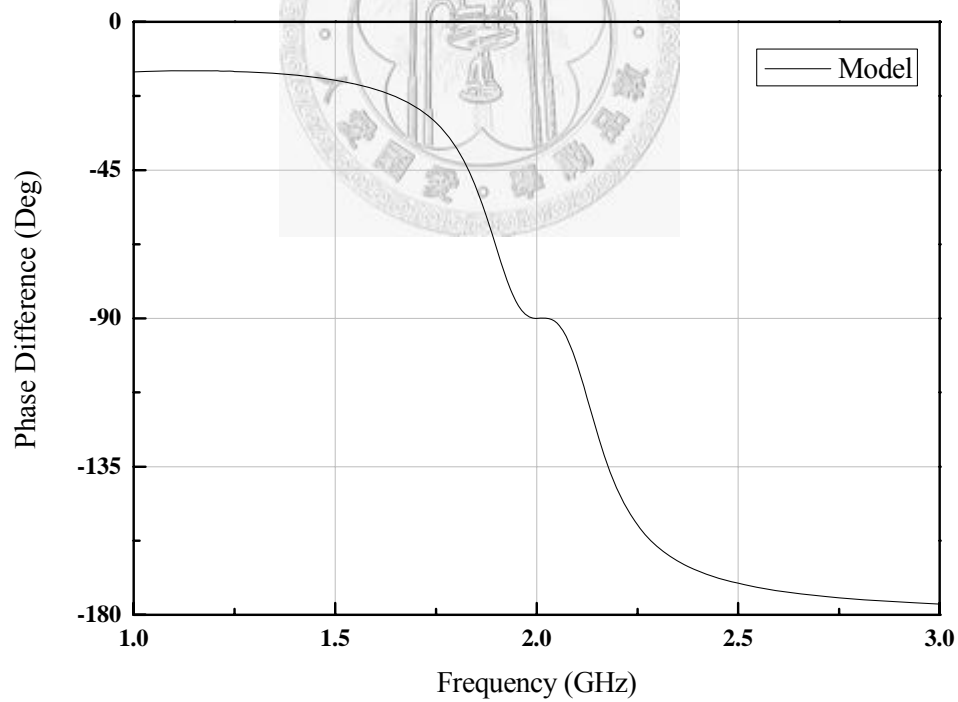


Fig. 4.9. Phase difference ($\angle S_{31} - \angle S_{21}$) of model with magnetic coupling

4.2 Design of Branch-Line Couplers with Coupled Resonators

In this section, we will demonstrate four coupler designs with different resonators. The first one uses traditional half-wavelength resonators and demonstrates this concept based on coupled resonators. The other designs use fork-like resonators which are evolved from net-type resonators. The circuit size reduces by 50% and achieves larger bandwidth at the same time. All three couplers are designed and fabricated using copper metallization on a Rogers RO4003 substrate with a relative dielectric constant of 3.38, a thickness of 0.508mm, and a loss tangent of 0.0027. These couplers are designed and simulated with full-wave simulator IE3D.

4.2.1 Coupler Design 1

Fig. 4.10 shows the layout of first coupler design, which is composed of four conventional half-wavelength resonators. The center frequency of the coupler is 2GHz. The coupling coefficients and external quality factors are chosen as

$$M_{12} = M_{34} = 0.0471,$$

$$M_{41} = M_{23} = 0.0333,$$

and

$$Q_e = 30.$$

Full-wave simulator IE3D has been used to extract above parameters. The coupling coefficients and external quality factor can be evaluated from the method presented in section 2.1. Fig. 4.11(a) plots the simulated coupling coefficients versus the distances between resonators, in which M_{12} , M_{23} , M_{34} , and M_{41} curves are the same because of symmetry of the structure. Fig. 4.11(b) plots the simulated external quality factor against the tapped line position. Although the resonators are different, the relationships between external quality factors and tapped position are almost the

same.

The design parameters of this coupler are $t_1 = t_2 = t_3 = t_4 = 2.8\text{mm}$, $d_{12} = d_{34} = 0.6\text{mm}$, $d_{23} = d_{41} = 0.8\text{mm}$, and $s = 16.6\text{mm}$. The circuit size of this coupler is around $47\text{mm} \times 16.1\text{mm}$, i.e., $0.5\lambda \times 0.18\lambda$.

Fig. 4.12 shows the photograph of the fabricated coupler. Fig. 4.13 and Fig. 4.14 show the simulated and measured data respectively. The comparisons between simulation and measurement are shown in Fig. 4.15, Fig. 4.16, Fig. 4.17, and Fig. 4.18. From the measured data, the return loss (S_{11}) $\geq 15\text{dB}$ in the frequency range of $1.98 \sim 2.01\text{ GHz}$, over which the magnitude of through port (S_{21}) is $-4.4 \sim -4.82\text{ dB}$ and the magnitude of coupled port (S_{31}) is $-5.26 \sim -5.43\text{ dB}$. The loss is contributed by dielectric loss and conductor loss. Take through port (S_{21}) as example. From the simulation result, it has a loss of 1.5 dB at center frequency. The dielectric loss contributes 0.5 dB , and the conductor loss contributes 1 dB . The phase difference between S_{21} and S_{31} is shown in Fig. 4.18. It has a phase difference of 90° at center frequency. Good agreement is observed between the simulation and measurement.

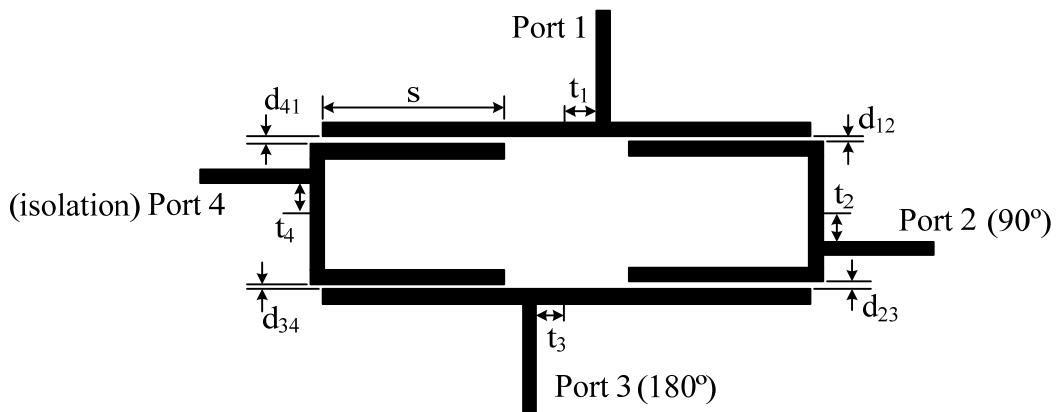


Fig. 4.10. Layout of coupler design 1

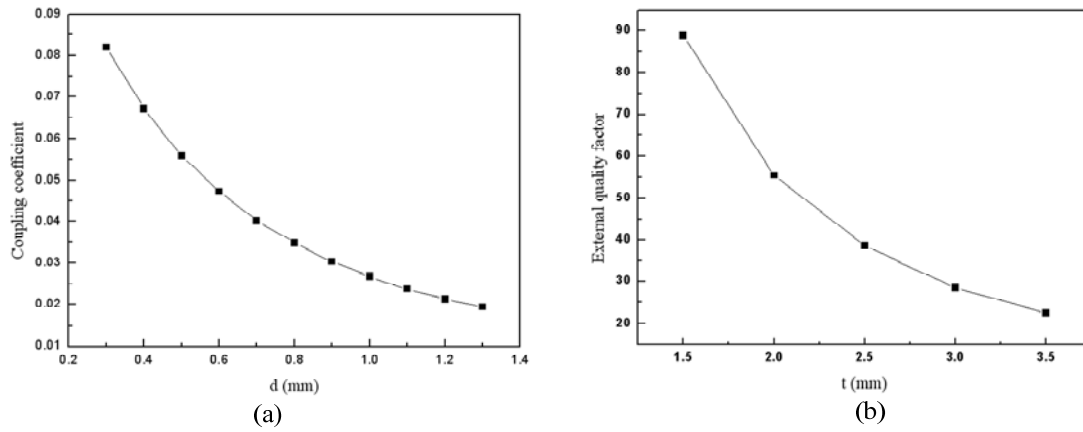


Fig. 4.11. Design features and characteristics for coupler design 1 in Fig. 4.10

(a) Coupling coefficient versus the distance between resonators

(b) External quality factor versus the tapped line position of resonator

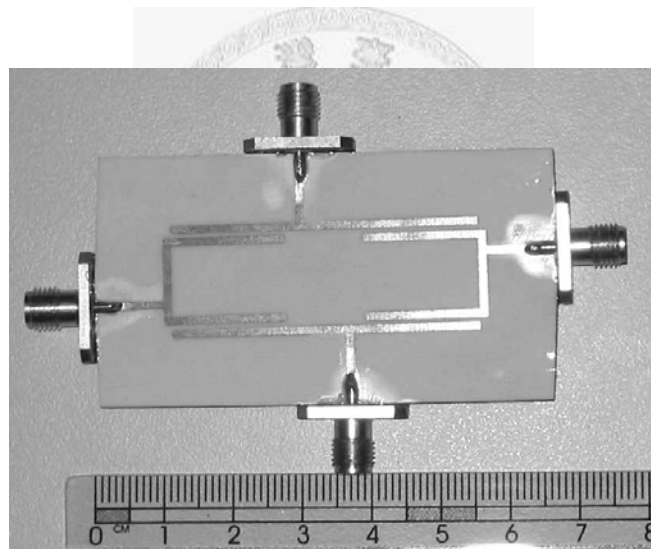


Fig. 4.12. Photograph of fabricated coupler design 1

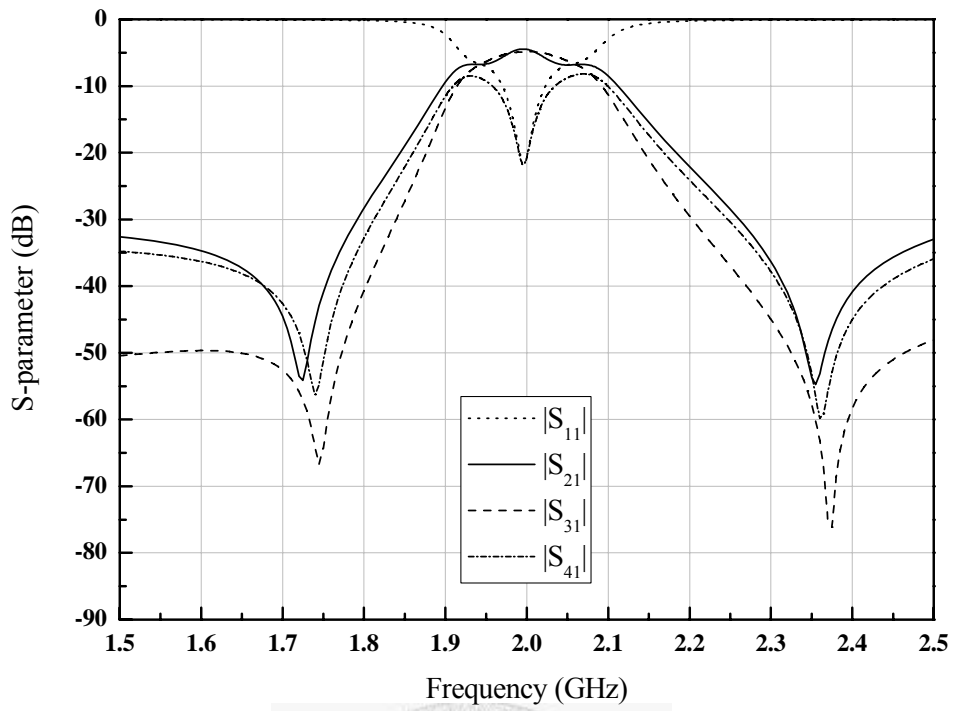


Fig. 4.13. Simulation result of coupler design 1

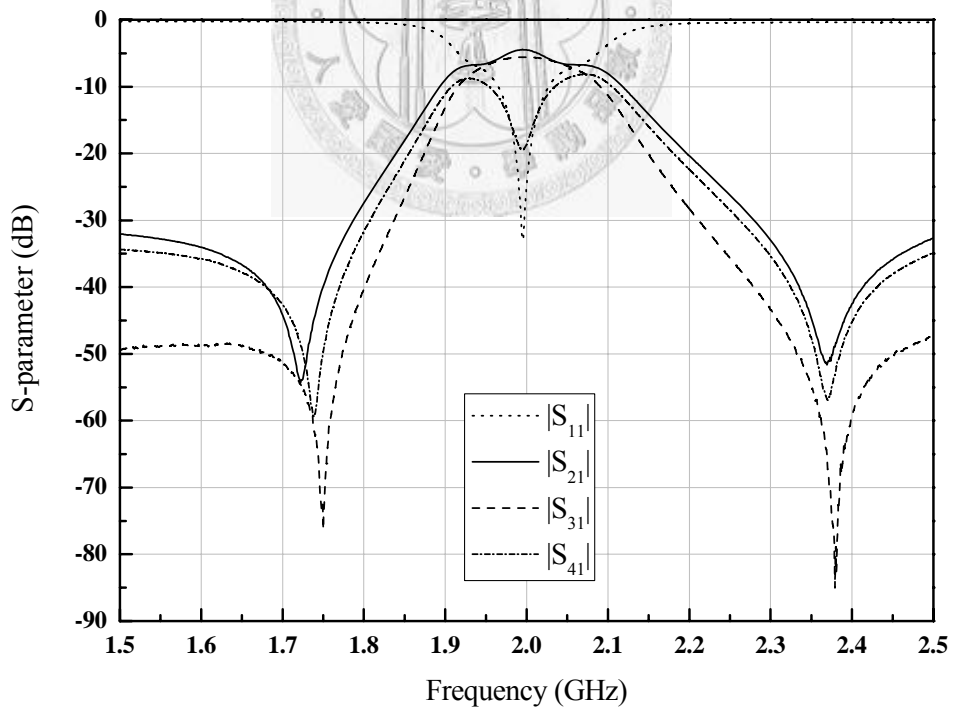


Fig. 4.14. Measurement result of coupler design 1

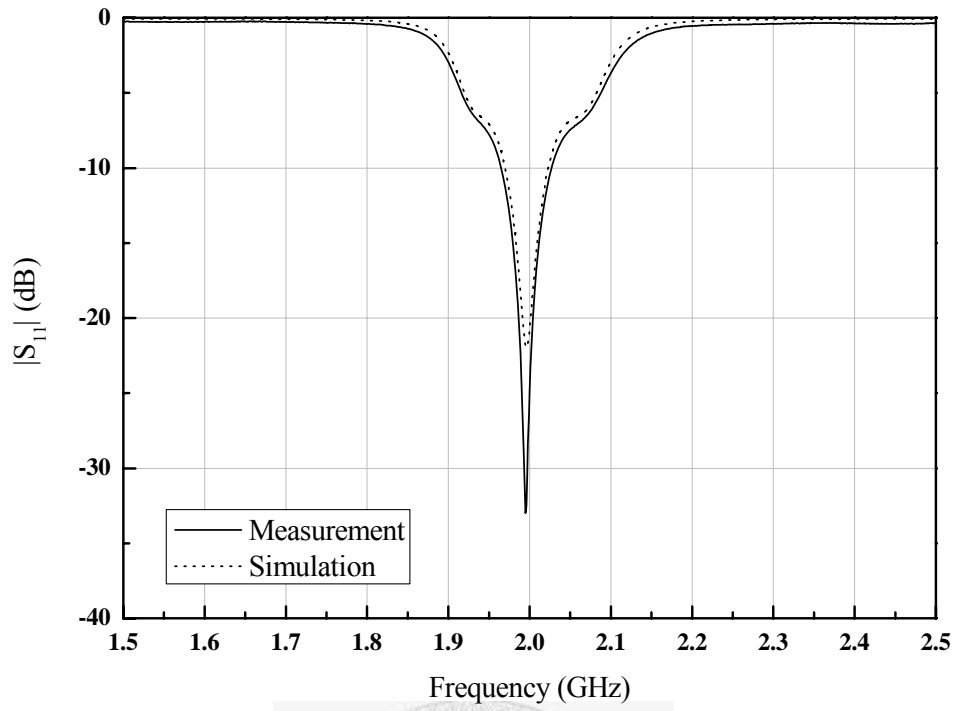


Fig. 4.15. Measured and simulated performances of coupler design 1 ($|S_{11}|$)

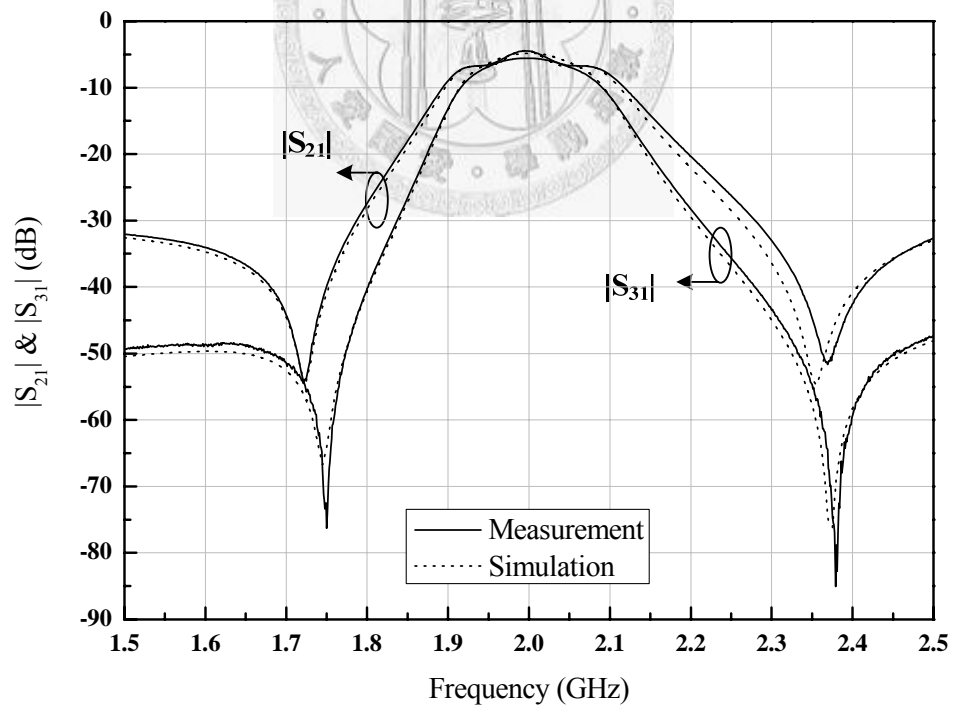


Fig. 4.16. Measured and simulated performances of coupler design 1 ($|S_{21}|$ & $|S_{31}|$)

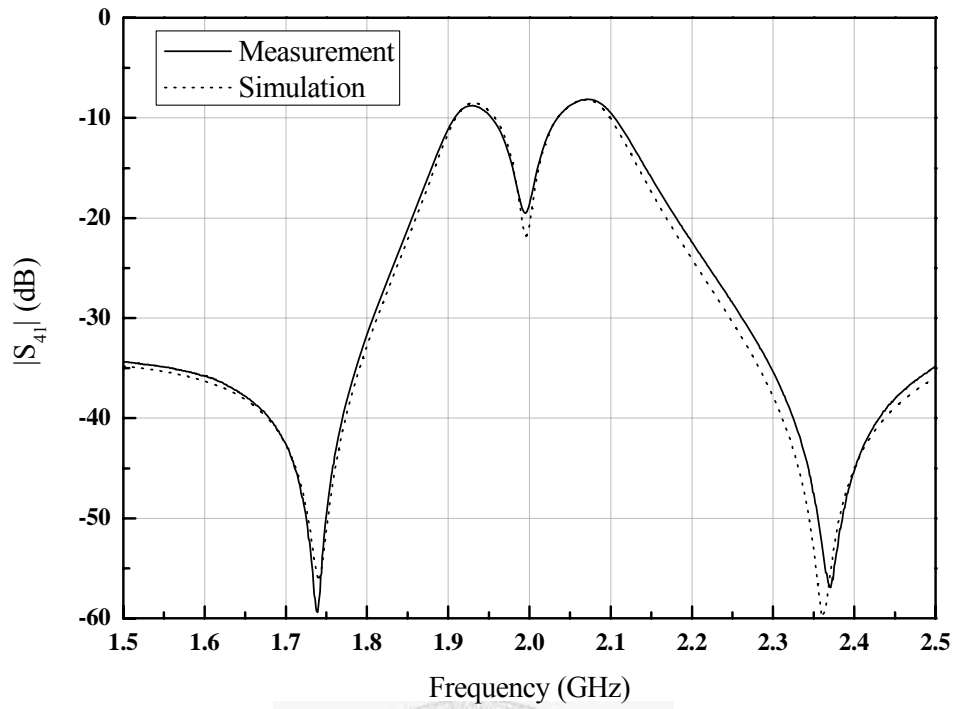


Fig. 4.17. Measured and simulated performances of coupler design 1 ($|S_{41}|$)

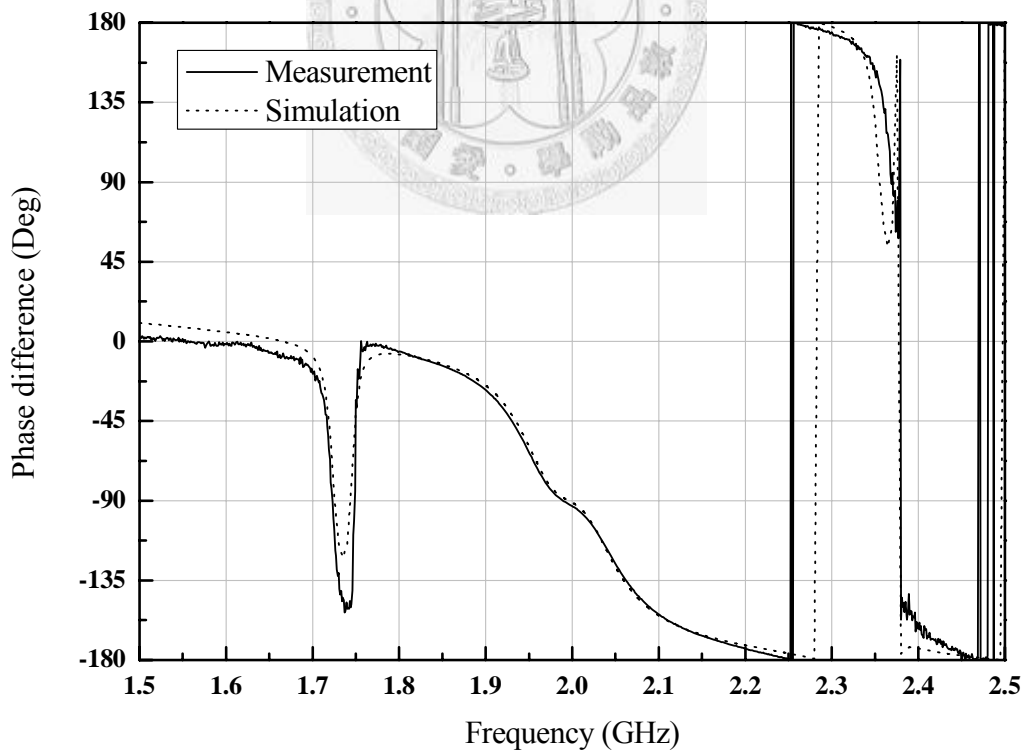


Fig. 4.18. Measured and simulated performances of coupler design 1 ($\angle S_{31} - \angle S_{21}$)

4.2.2 Coupler Design 2

In order to reduce the circuit size, the concept of net-type resonator is adopted. Fig. 4.19 illustrates the procedure of resonator design. Low impedance transmission-line sections in Fig. 4.19(a) are replaced with several joint-connected high impedance transmission-line sections as shown in Fig. 4.19(b). In order to further reduce the size, central high impedance transmission-line section is meandered (Fig. 4.19(c), (d)). This structure reduces circuit size and increases available coupling coefficient at the same time. Although the structure is slightly changed from original net-type resonator, the design formulations described in the previous chapter are still available.

Fig. 4.20 shows the layout of the second coupler design, which consists of four fork-like resonators illustrated in Fig. 4.19. The central frequency of this coupler is designed at 2GHz. The coupling coefficients and external quality factor are chosen as

$$M_{12} = M_{34} = 0.14 ,$$

$$M_{41} = M_{23} = 0.10 ,$$

and

$$Q_e = 10 .$$

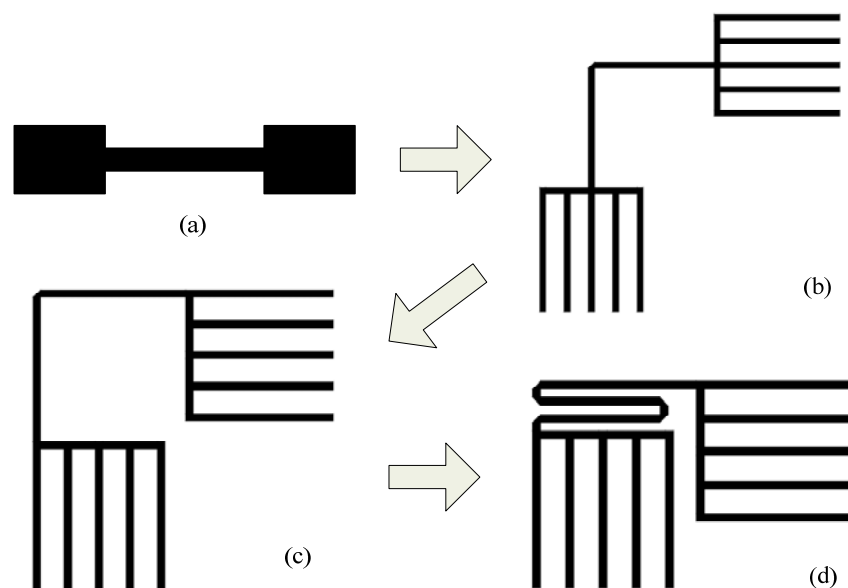


Fig. 4.19. The procedure of resonator design

Full-wave simulator IE3D has been used to extract the above parameters. The coupling coefficients and external quality factor can be evaluated from the method presented in section 2.1. Fig. 4.21(a) plots the simulated coupling coefficients versus the distances between resonators, in which M_{12} , M_{23} , M_{34} , and M_{41} curves are the same. Fig. 4.21(b) plots the simulated external quality factor against the tapped line position.

The design parameters illustrated in Fig. 4.20 are $t_1 = t_2 = t_3 = t_4 = 2.25\text{mm}$, $d_{12} = d_{34} = 0.35\text{mm}$, and $d_{23} = d_{41} = 1.05\text{mm}$. The parameters of each resonator are listed in Table 4.1. Although the original design is fully symmetric, the sizes of resonators are slightly changed after optimization. The circuit size of this coupler is around $14.9\text{mm} \times 15.6\text{mm}$, i.e., $0.17\lambda \times 0.175\lambda$. It only occupies 48% of area of traditional branch-line coupler.

Fig. 4.22 shows the photograph of the fabricated coupler. Fig. 4.23 and Fig. 4.24 show the simulated and measured data respectively. The comparisons of simulation and measurement are shown in Fig. 4.25, Fig. 4.26, Fig. 4.27, and Fig. 4.28. The central frequency of fabricated circuit is shifted to 2.047GHz (according to the minimum of S_{11}). From the measured data, the return loss (S_{11}) $\geq 15\text{dB}$ in the frequency range of 2 ~ 2.09 GHz, over which the magnitude of through port (S_{21}) is -4.3 ~ -4.9 dB and the magnitude of coupled port (S_{31}) is -3.85 ~ 4.08 dB. The phase difference between S_{21} and S_{31} is shown in Fig. 4.28.

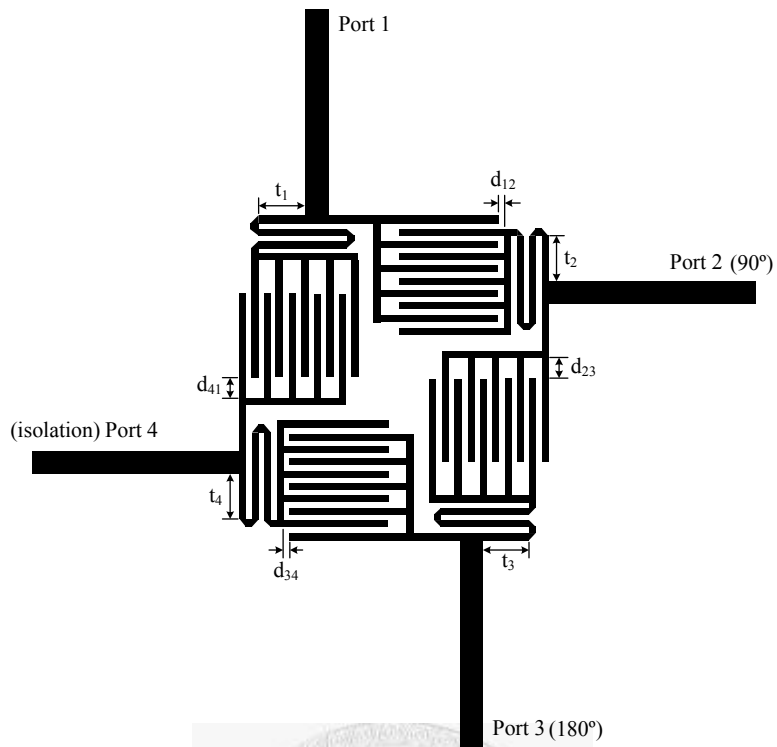


Fig. 4.20. Layout of coupler design 2

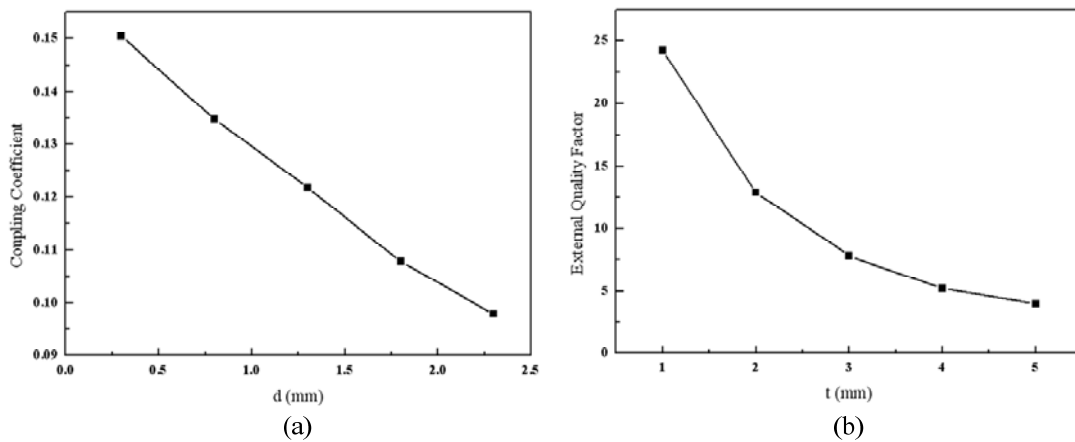


Fig. 4.21. Design features and characteristics for coupler design 2 in Fig. 4.20

(a) Coupling coefficient versus the distance between resonators

(b) External quality factor versus the tapped line position of resonator

Table 4.1 Parameters of designed resonators (coupler design 2)

	Initial Value	Resonator 1/3	Resonator 2/4
w	0.3 mm	0.3 mm	0.3 mm
L_1	11.3 mm	11.55 mm	10.95 mm
L_2	4.3 mm	4.3 mm	4.3 mm
L_3	6 mm	6.25 mm	5.65 mm
L_4	5.7mm	5.95mm	5.35mm
g_1	0.9 mm	0.9 mm	0.9 mm
g_2	0.3 mm	0.3 mm	0.3 mm

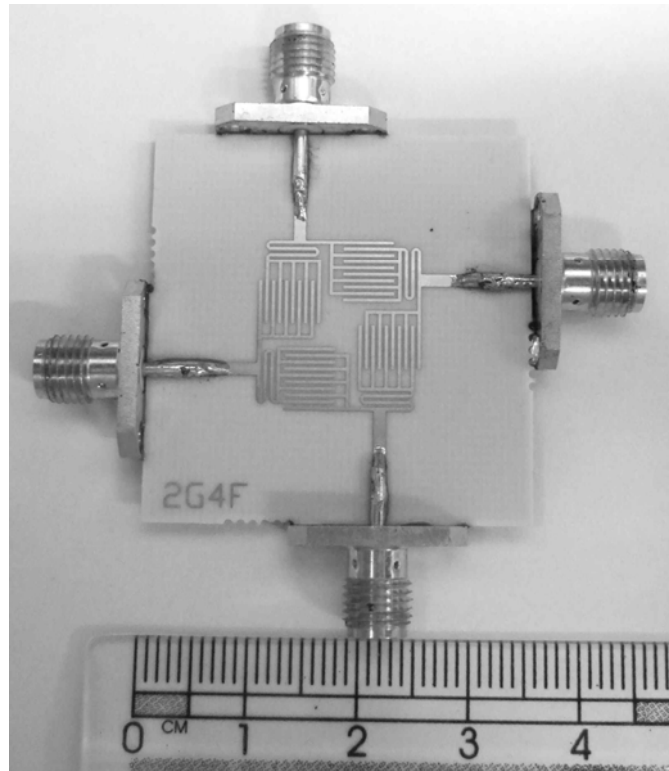


Fig. 4.22. Photograph of fabricated coupler design 2

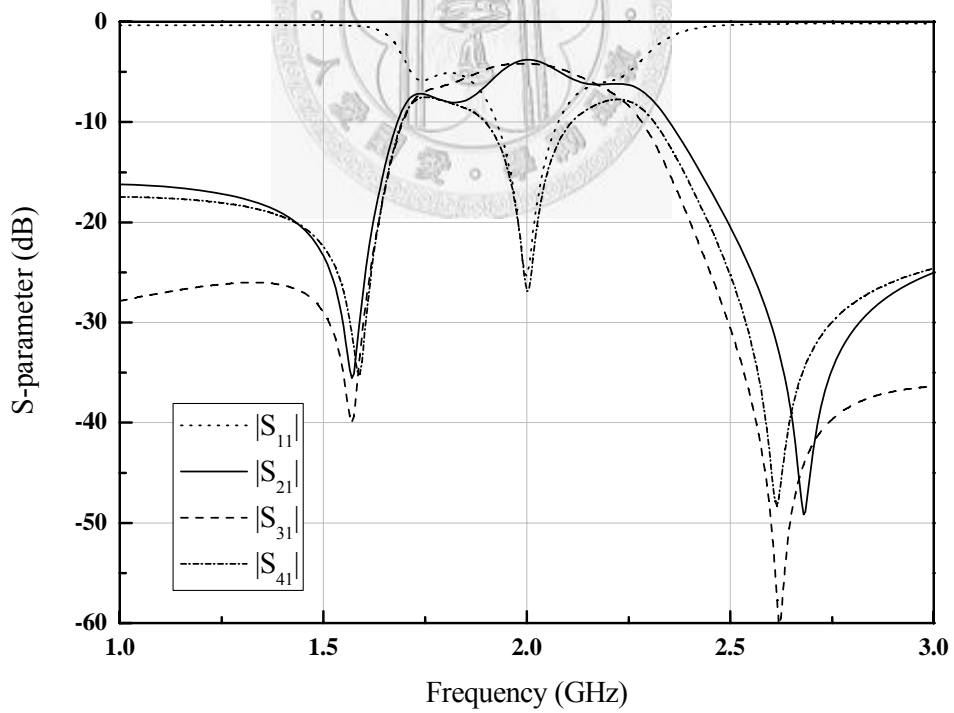


Fig. 4.23. Simulation result of coupler design 2

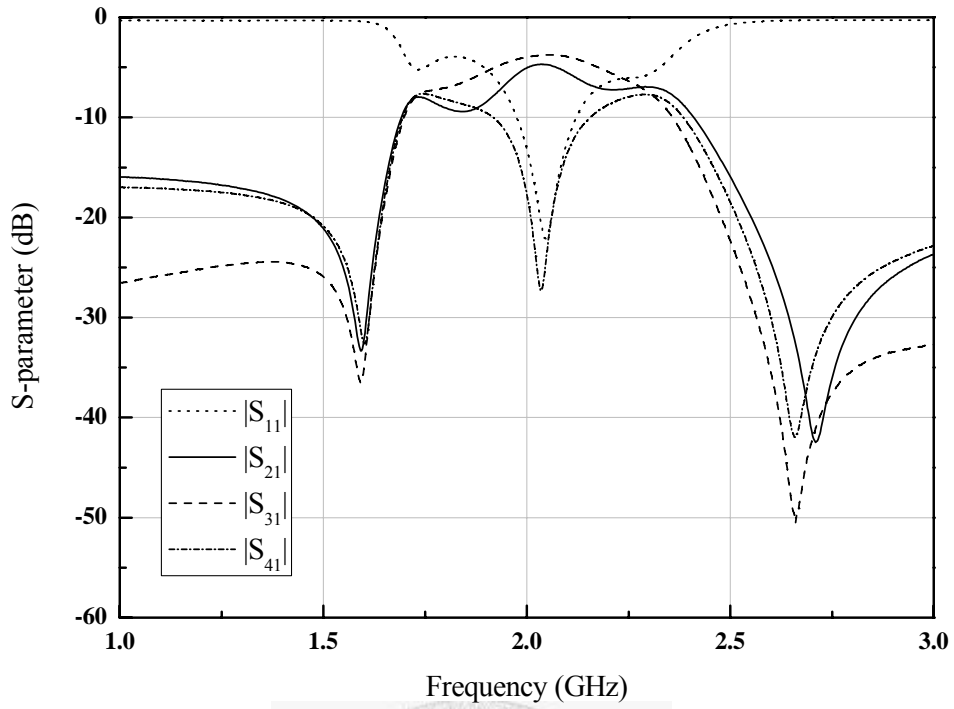


Fig. 4.24. Measurement of coupler design 2

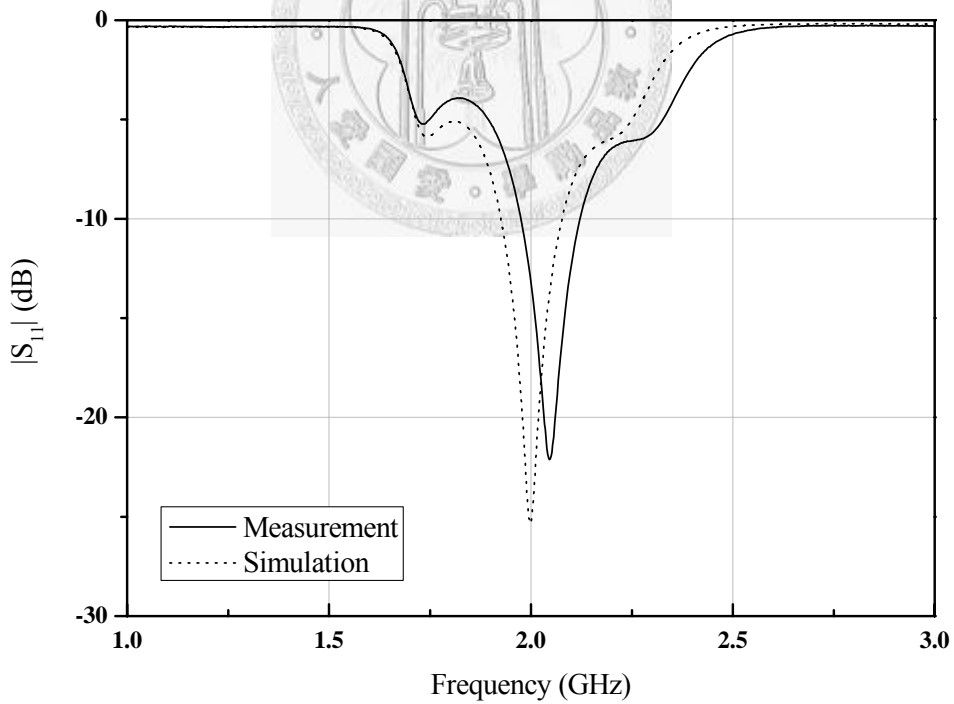


Fig. 4.25. Measured and simulated performances of coupler design 2 ($|S_{11}|$)

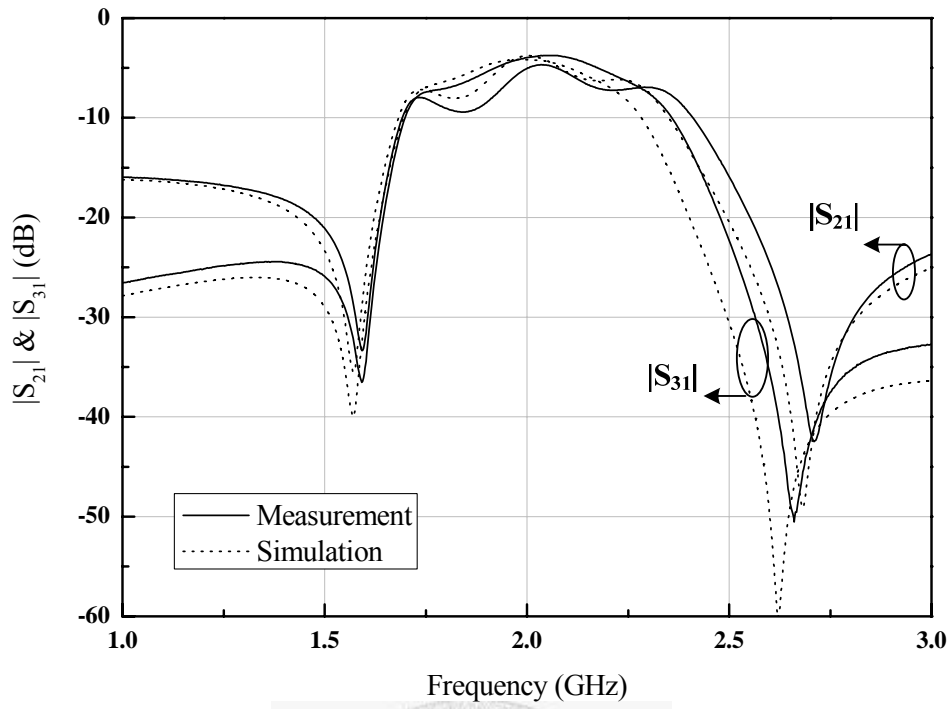


Fig. 4.26. Measured and simulated performances of coupler design 2 ($|S_{21}|$ & $|S_{31}|$)

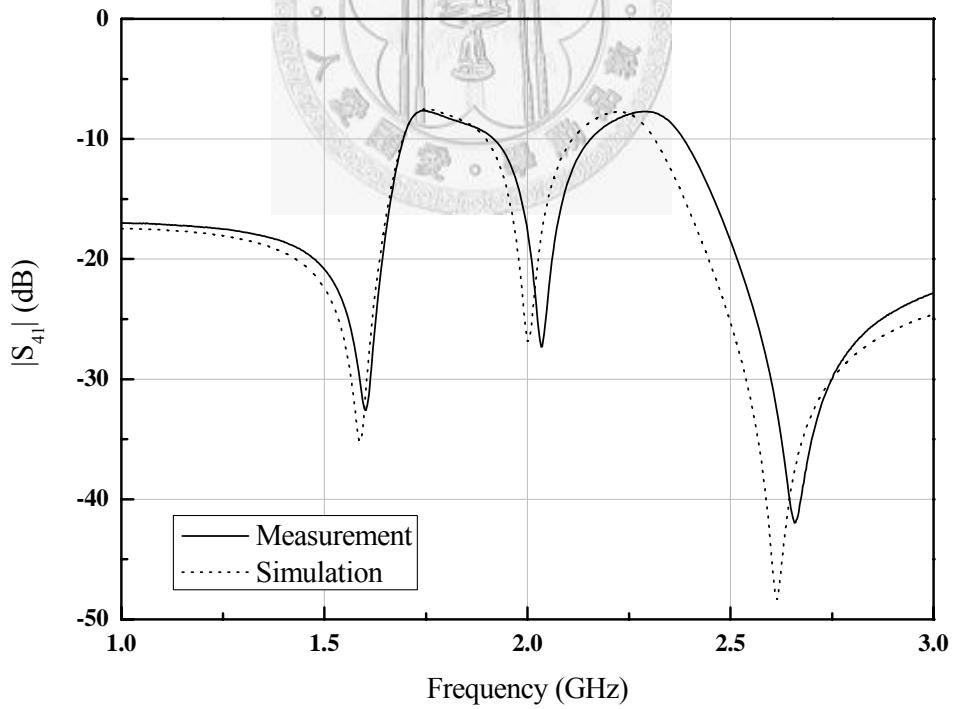


Fig. 4.27. Measured and simulated performances of coupler design 2 ($|S_{41}|$)

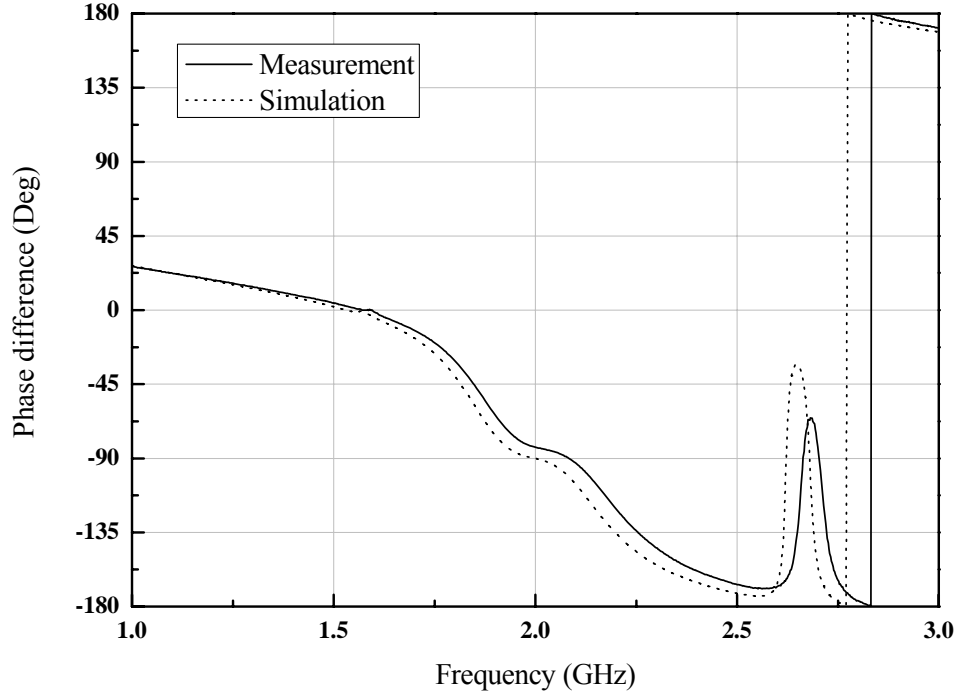


Fig. 4.28. Measured and simulated performances of coupler design 2 ($\angle S_{31} - \angle S_{21}$)

4.2.3 Coupler design 3

In general, the meander line in the previous design is undesired because it usually accompanies some non-ideal effects. In this design, we increase the number of fingers and remove the meander lines. Although the impedance ratio of resonators increases, but its length is only slightly reduces, i.e. the size of whole coupler does not reduce compared with the previous design.

Fig. 4.29 shows the layout of the third coupler design. The central frequency of this coupler is designed at 2GHz. The coupling coefficients and external quality factor are chosen as

$$M_{12} = M_{34} = 0.148,$$

$$M_{41} = M_{23} = 0.104,$$

and

$$Q_e = 9.6.$$

Full-wave simulator IE3D has been used to extract the above parameters. Fig. 4.30(a) plots the simulated coupling coefficients versus the distances between resonators, in which M_{12} , M_{23} , M_{34} , and M_{41} curves are the same. Fig. 4.30(b) plots the simulated external quality factor against the tapped line position.

The design parameters illustrated in Fig. 4.29 are $t_1 = t_2 = t_3 = t_4 = 6.3\text{mm}$, $d_{12} = d_{34} = 0.65\text{mm}$, and $d_{23} = d_{41} = 1.65\text{mm}$. The parameters of each resonator are listed in Table 4.2. Although the original design is fully symmetric, the sizes of resonators are slightly changed after optimization. The circuit size of this coupler is around $15.6\text{mm} \times 16.2\text{mm}$, i.e., $0.175\lambda \times 0.18\lambda$. It occupies 50% of area of traditional branch-line coupler.

Fig. 4.31 shows the photograph of the fabricated coupler. Fig. 4.32 and Fig. 4.33 show the simulation result and measured data respectively. The measured data meet the simulation result very well. From the measured data, the return loss ($|S_{11}|$) $\geq 15\text{dB}$ in the frequency range of $1.96 \sim 2.04\text{GHz}$, over which the magnitude of through port ($|S_{21}|$) is $-3.9 \sim -4.4\text{dB}$ and the magnitude of coupled port ($|S_{31}|$) is $-3.5 \sim -3.75\text{dB}$. The phase difference between through port and coupled port is shown in Fig. 4.37. They have 90° phase difference near center frequency.

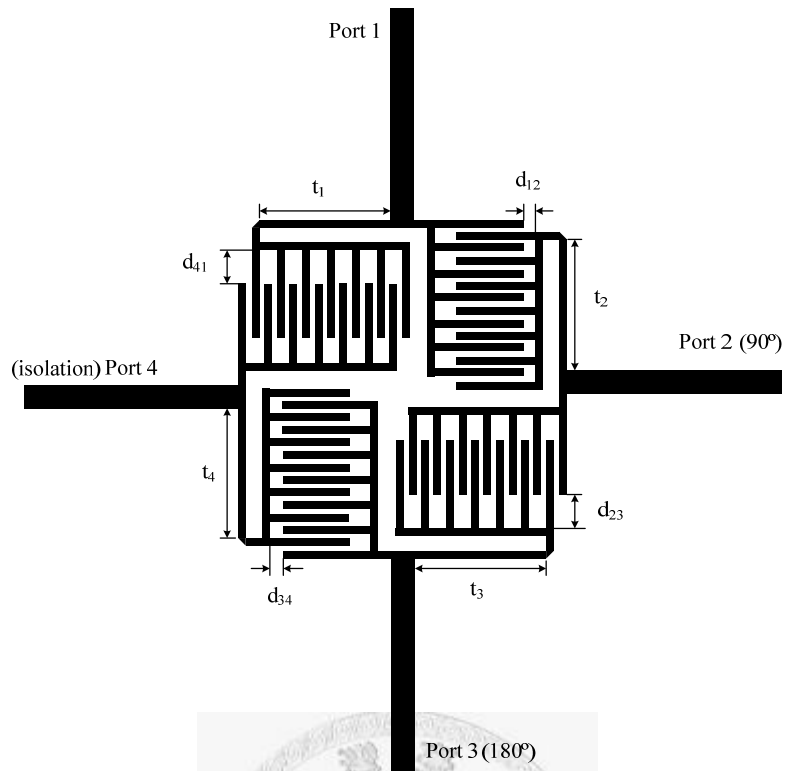


Fig. 4.29. Layout of coupler design 3

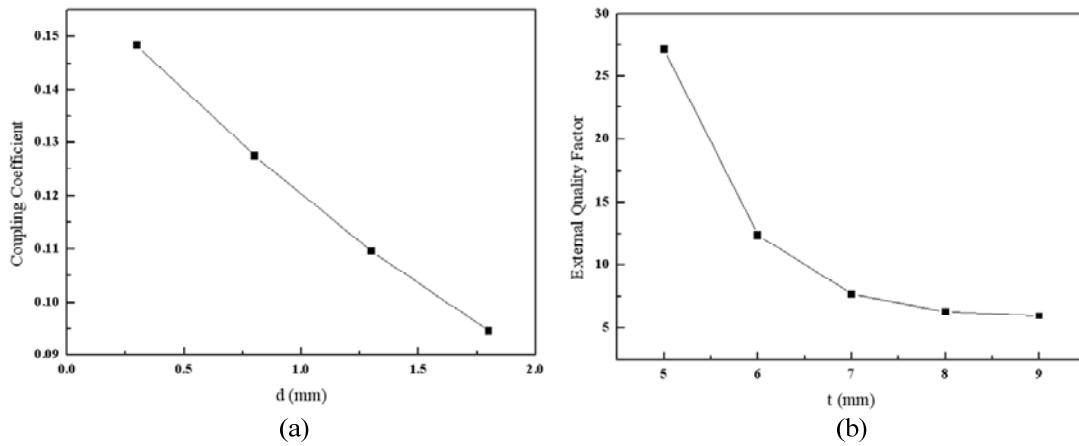
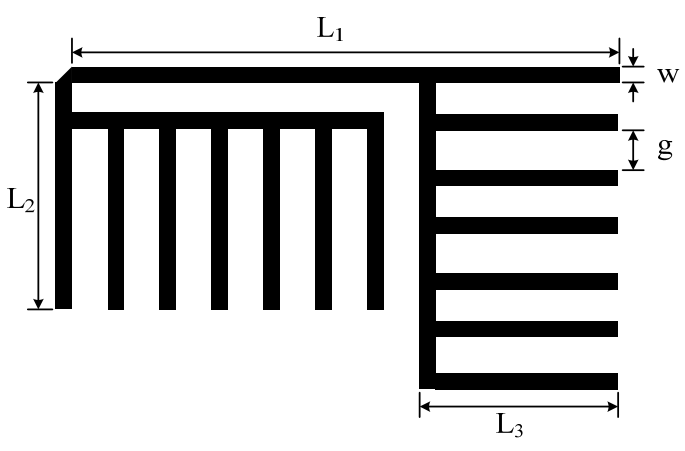


Fig. 4.30. Design features and characteristics for coupler design 3 in Fig. 4.29

(a) Coupling coefficient versus the distance between resonators

(b) External quality factor versus the tapped line position of resonator

Table 4.2 Parameters of designed resonators (coupler design 3)



	Initial Value	Resonator 1/3	Resonator 2/4
w	0.3 mm	0.3 mm	0.3 mm
L ₁	12.5 mm	12.65 mm	12.25 mm
L ₂	5.2 mm	5.35 mm	4.95 mm
L ₃	4.4 mm	4.55 mm	4.15 mm
g	0.9 mm	0.9 mm	0.9 mm

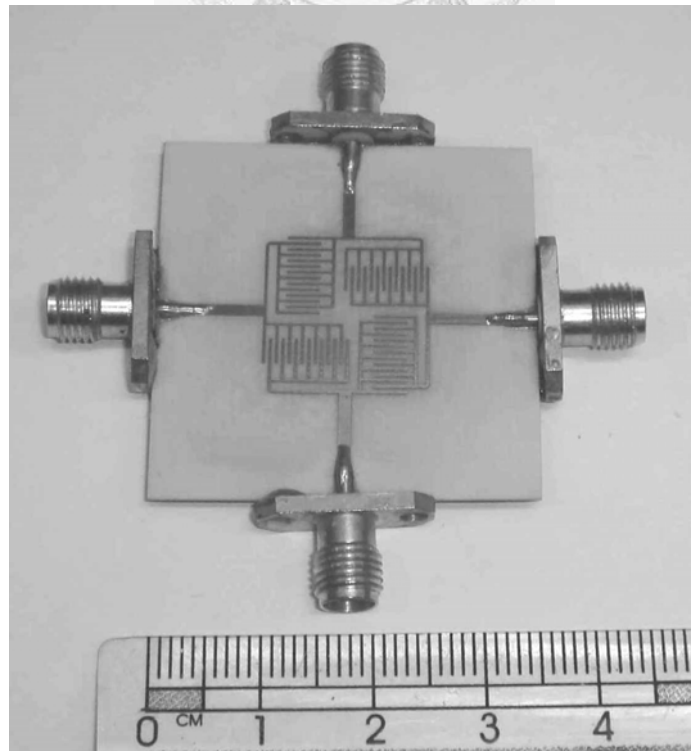


Fig. 4.31. Photograph of fabricated coupler design 3

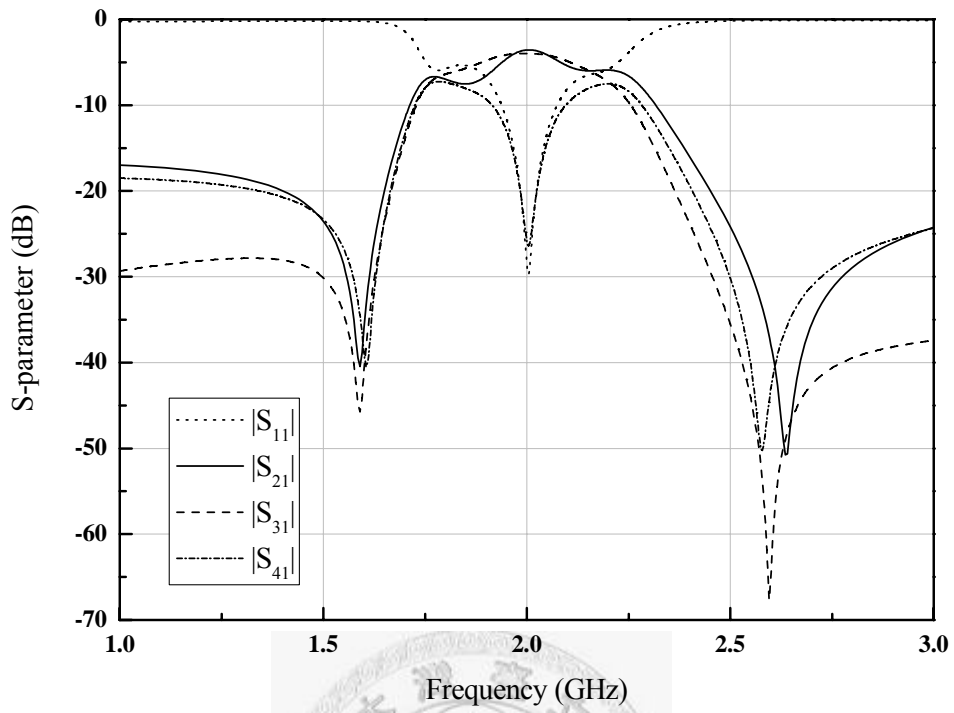


Fig. 4.32. Simulation result of coupler design 3

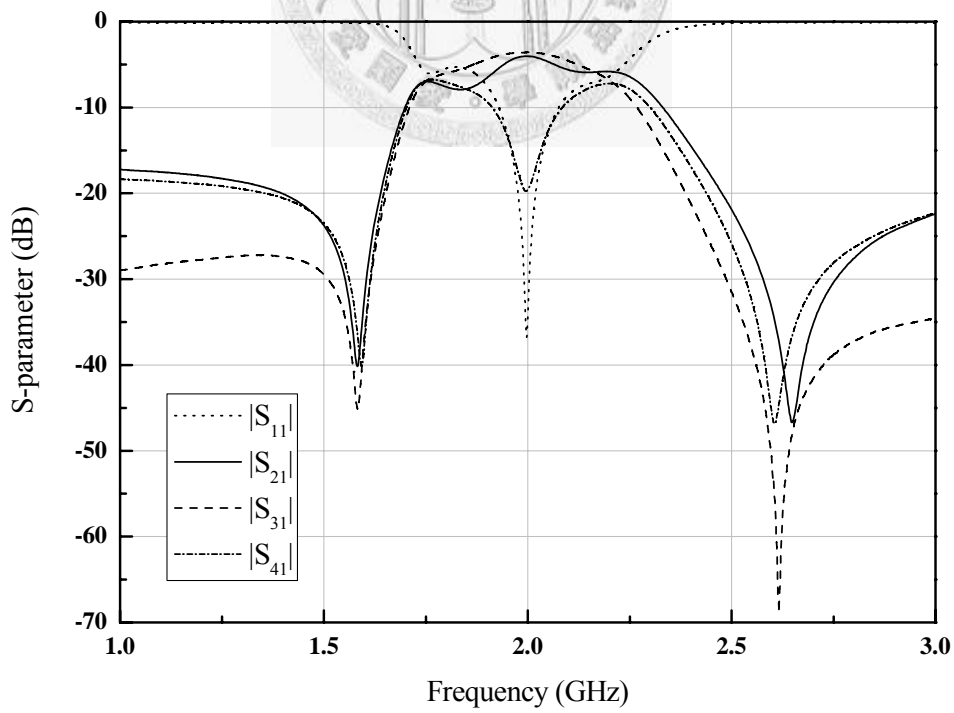


Fig. 4.33. Measurement of coupler design 3

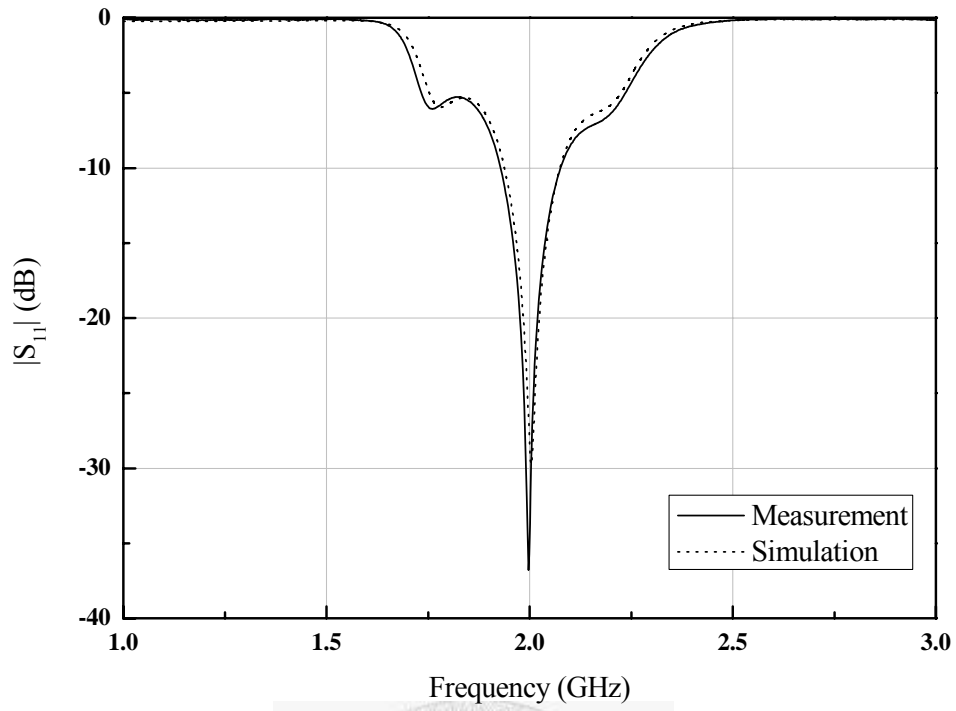


Fig. 4.34. Measured and simulated performances of coupler design 3 ($|S_{11}|$)

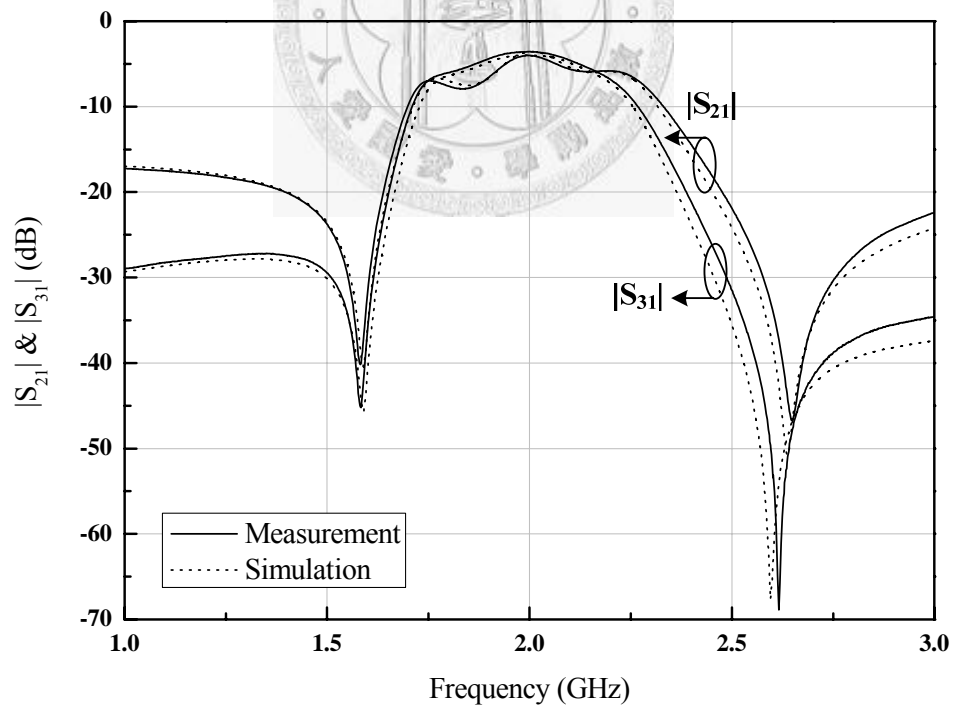


Fig. 4.35. Measured and simulated performances of coupler design 3 ($|S_{21}|$ & $|S_{31}|$)

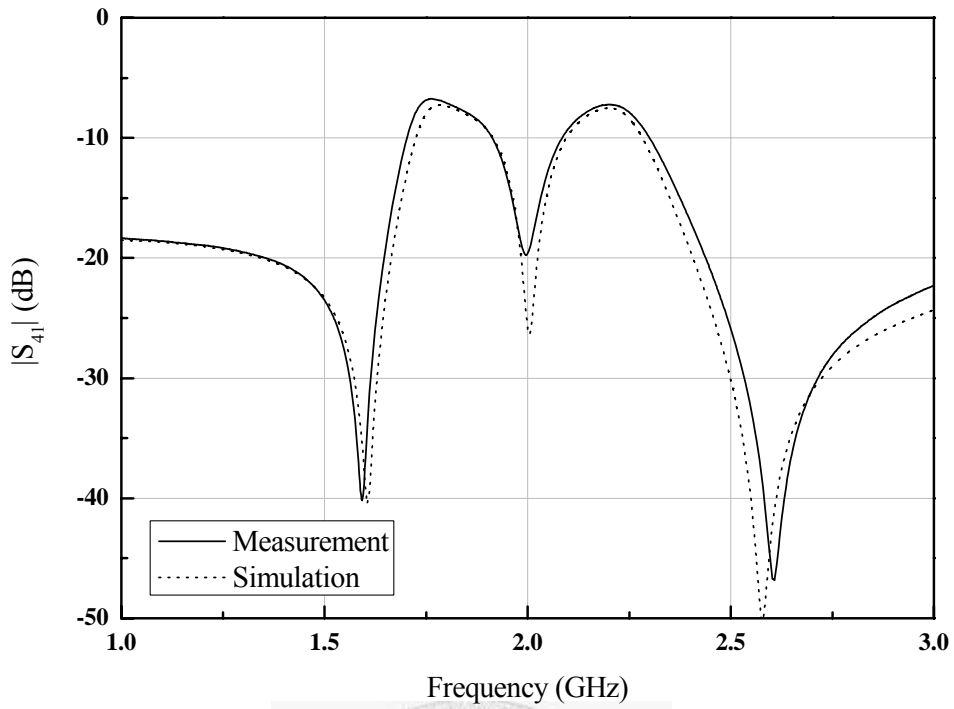


Fig. 4.36. Measured and simulated performances of coupler design 3 ($|S_{41}|$)

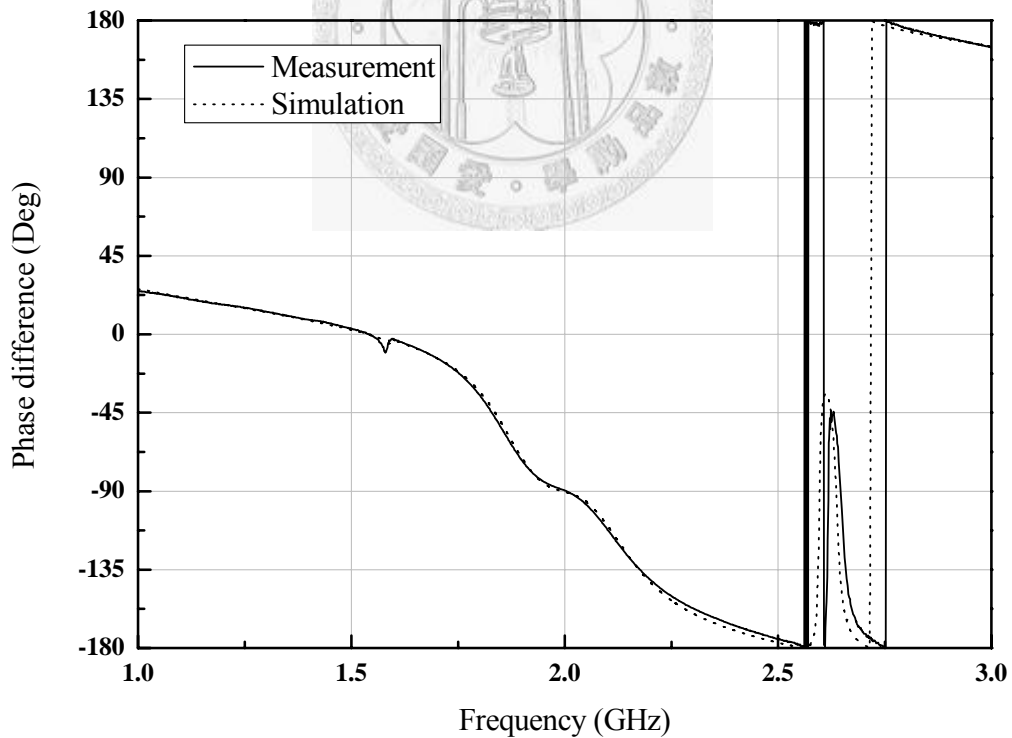


Fig. 4.37. Measurement and simulation result of coupler design 3 ($\angle S_{31} - \angle S_{21}$)

4.2.4 Coupler design 4

In order to get wider bandwidth, thinner microstrip line is adopted in this design. Fig. 4.38 shows the layout of the fourth coupler design. The width of microstrip used in resonators is 0.2mm.

The central frequency of this coupler is also designed at 2GHz. The coupling coefficients and external quality factor are chosen as

$$M_{12} = M_{34} = 0.205 ,$$

$$M_{41} = M_{23} = 0.145 ,$$

and

$$Q_e = 6.9 .$$

Full-wave simulator IE3D has been used to extract the above parameters. Fig. 4.39(a) plots the simulated coupling coefficients versus the distances between resonators, in which M_{12} , M_{23} , M_{34} , and M_{41} curves are the same. Fig. 4.39(b) plots the simulated external quality factor against the tapped line position.

The design parameters illustrated in Fig. 4.38 are $t_1 = t_2 = t_3 = t_4 = 4.4mm$, $d_{12} = d_{34} = 0.55mm$, and $d_{23} = d_{41} = 1.6mm$. The parameters of each resonator are listed in Table 4.3. As the third design, the sizes of each resonator are slightly changed after optimization. The circuit size of this coupler is around $14.6mm \times 14.9mm$, i.e., $0.16\lambda \times 0.165\lambda$. It occupies only 42% of area of traditional branch-line coupler.

Fig. 4.40 shows the photograph of the fabricated coupler. Fig. 4.41 and Fig. 4.42 show the simulation result and measured data respectively. The comparisons of simulation and measurement are shown in Fig. 4.43, Fig. 4.44, Fig. 4.45, and Fig. 4.46. The central frequency is slightly shifted. From the measured data, the return loss ($|S_{11}|$) ≥ 15 dB in the frequency range of 1.94 ~ 2.04 GHz, over which the magnitude of through port ($|S_{21}|$) is -4.4 ~ -4.8 dB and the magnitude of coupled port ($|S_{31}|$) is -3.4 ~ -3.6 dB. The phase difference between through port and coupled port is shown

in Fig. 4.46. The response is also slightly shifted.

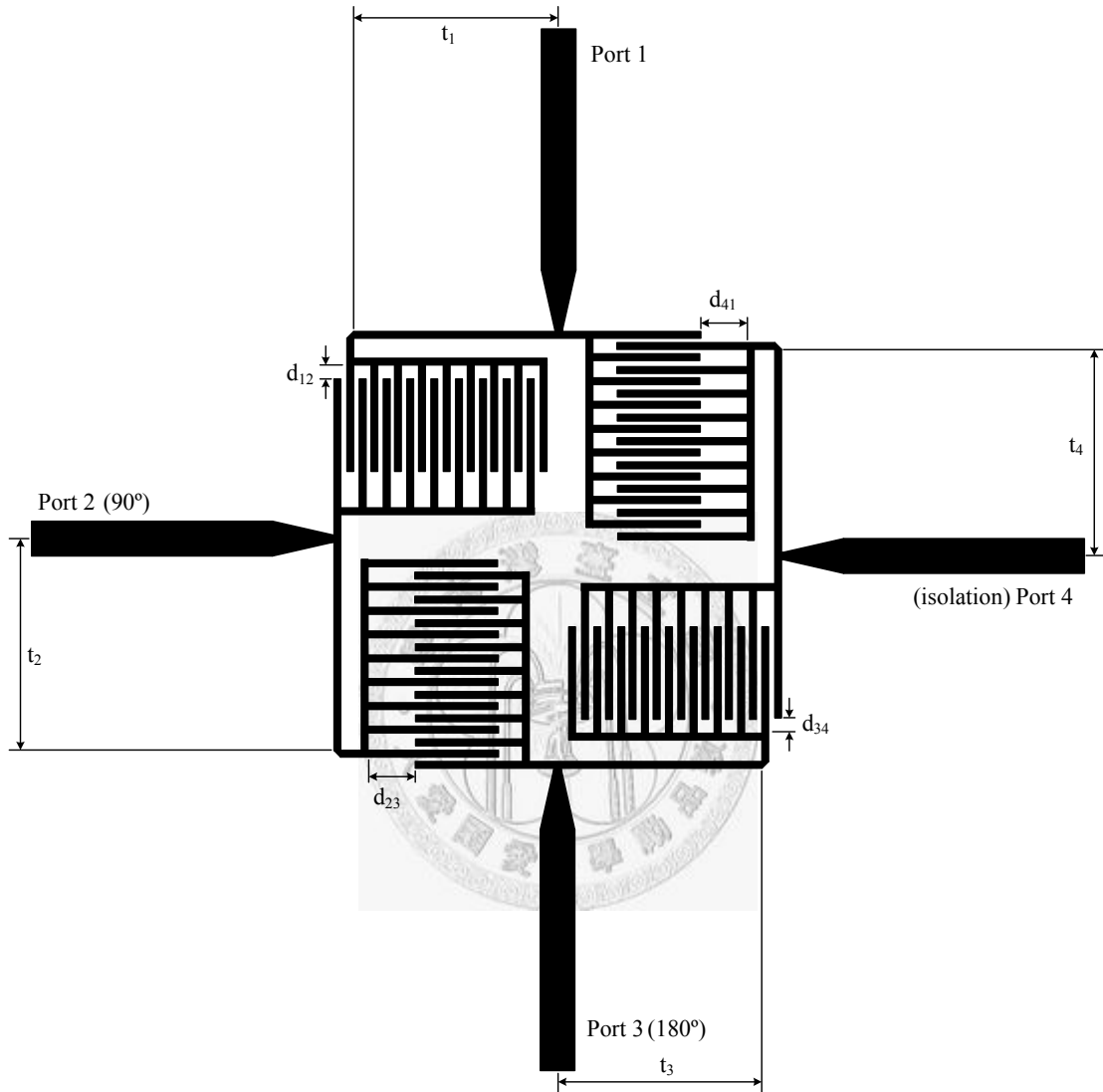


Fig. 4.38. Layout of coupler design 4

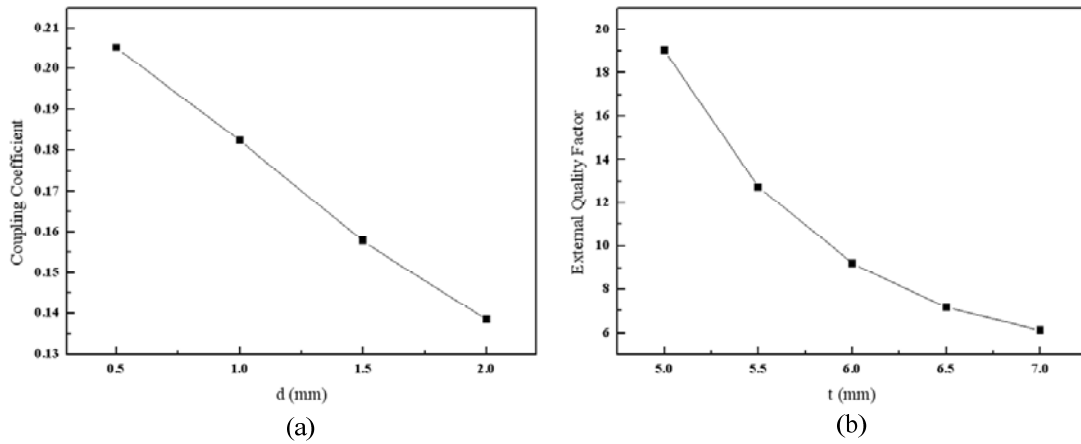


Fig. 4.39. Design features and characteristics for coupler design 4 in Fig. 4.38
 (a) Coupling coefficient versus the distance between resonators
 (b) External quality factor versus the tapped line position of resonator

Table 4.3 Parameters of designed resonators (coupler design 4)

The schematic diagram shows a coupler design with two resonators. The left resonator has a length L_1 and a width w . The right resonator has a length L_3 and a width w . The distance between the resonators is L_2 . The gap between the resonators is g .

	Initial Value	Resonator 1/3	Resonator 2/4
w	0.2 mm	0.2 mm	0.2 mm
L_1	12.15 mm	11.55 mm	12.3 mm
L_2	5.05 mm	4.45 mm	5.2 mm
L_3	4.35 mm	3.75 mm	4.5 mm
g	0.6 mm	0.6 mm	0.6 mm

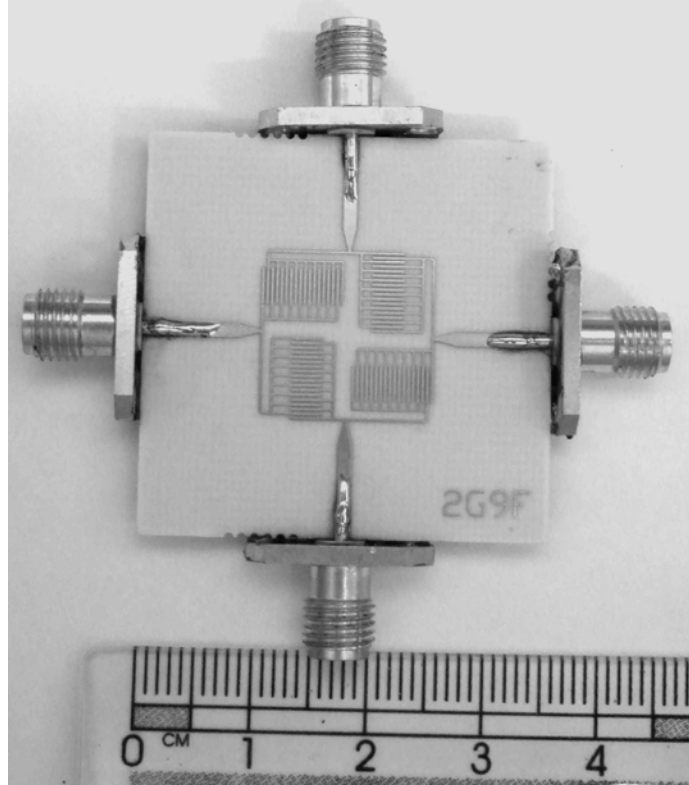


Fig. 4.40. Photograph of fabricated coupler design 4

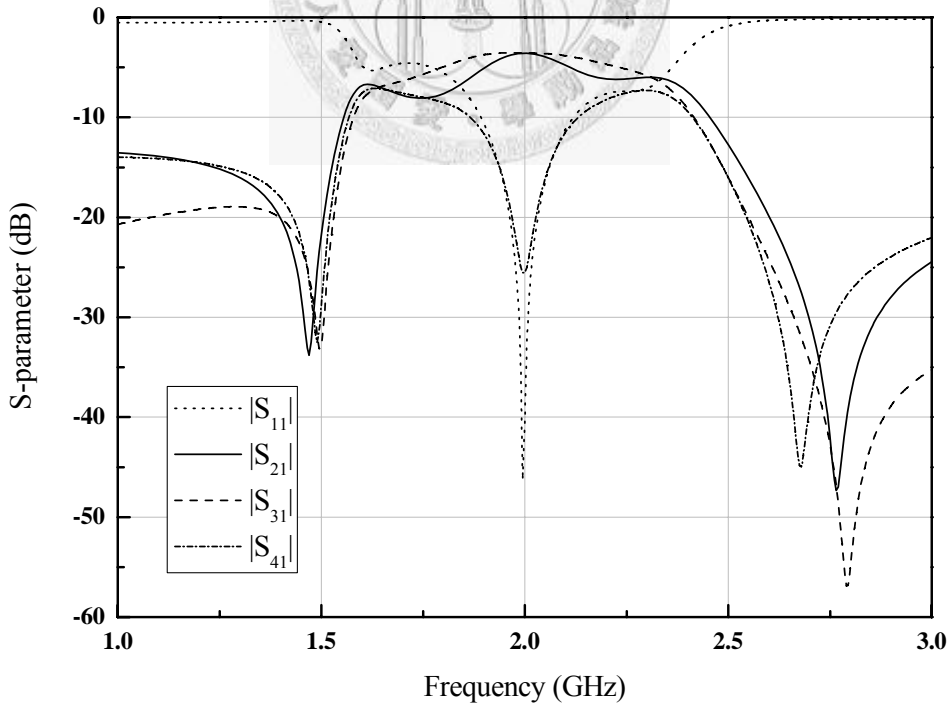


Fig. 4.41. Simulation result of coupler design 4

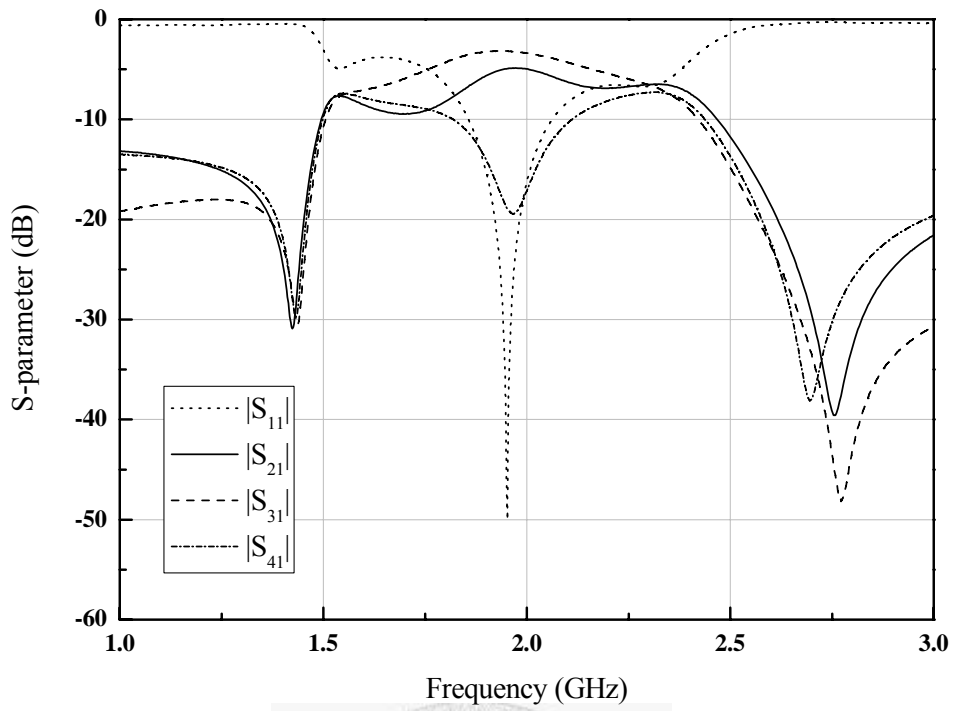


Fig. 4.42. Measurement of coupler design 4

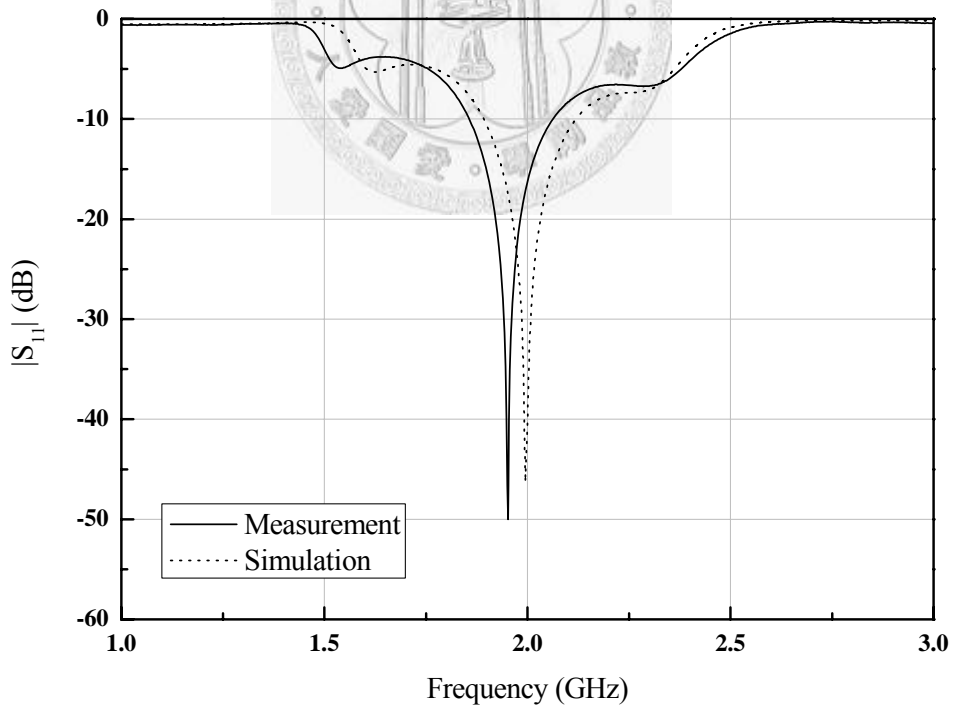


Fig. 4.43. Measured and simulated performances of coupler design 4 ($|S_{11}|$)

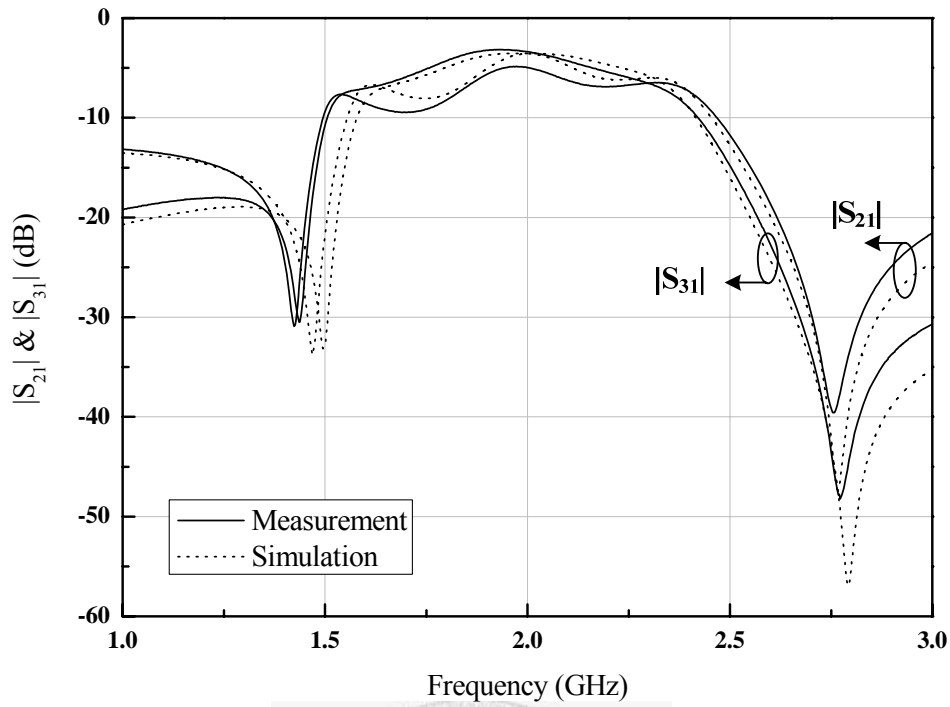


Fig. 4.44. Measured and simulated performances of coupler design 4 ($|S_{21}|$ & $|S_{31}|$)

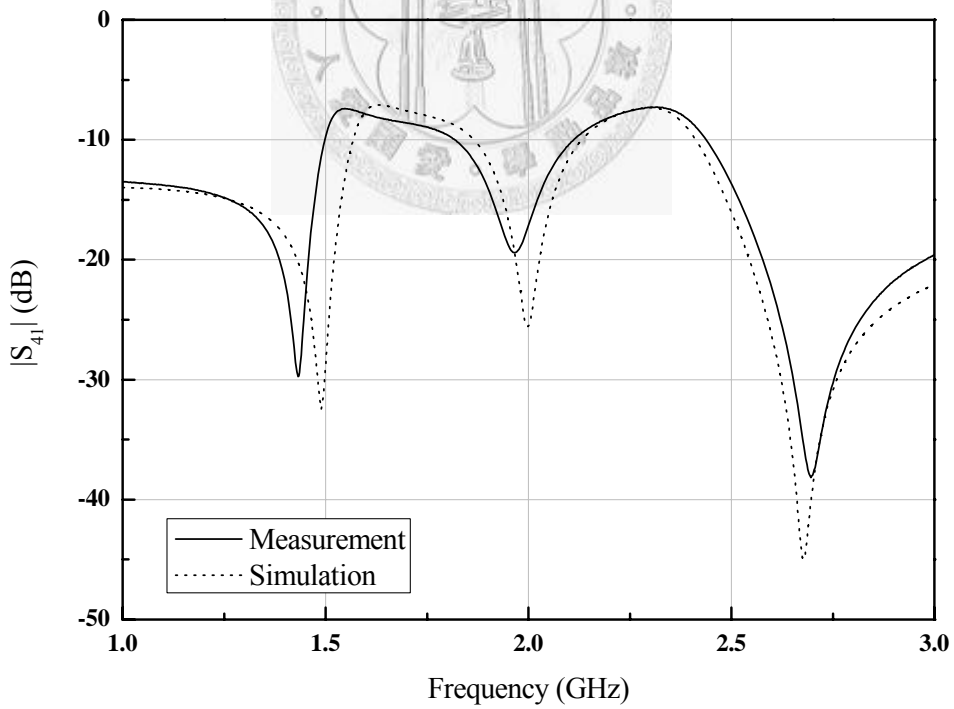


Fig. 4.45. Measured and simulated performances of coupler design 4 ($|S_{41}|$)

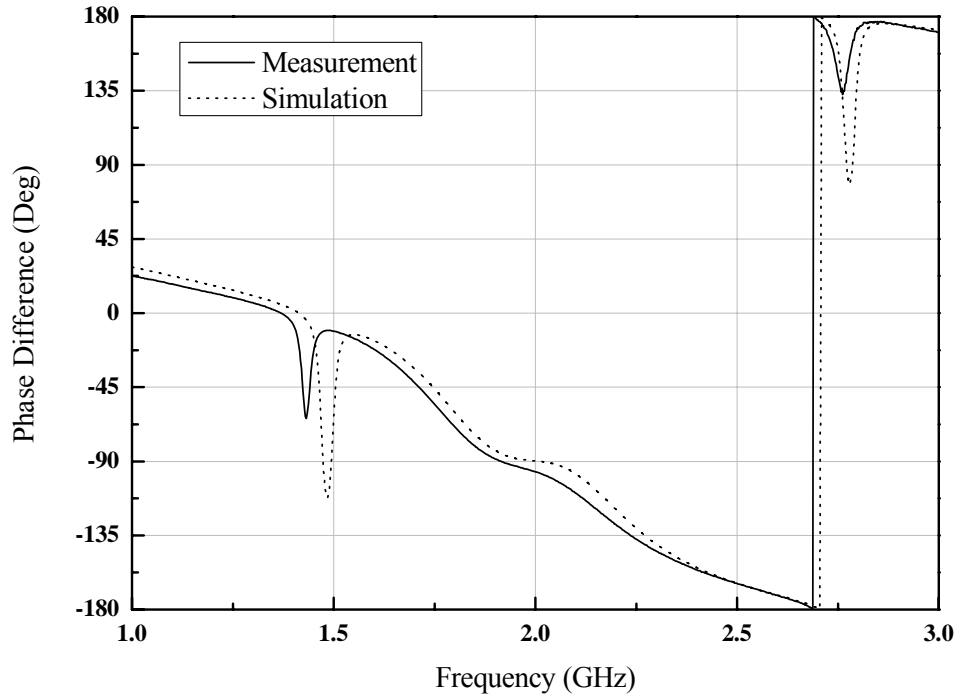


Fig. 4.46. Measurement and simulation results of coupler design 4 ($\angle S_{31} - \angle S_{21}$)

4.2.5 Dual-band coupler

In this section, the idea of transforming branch-line coupler into coupled-resonator network is extended to dual-band design. With stepped-impedance resonators, a dual-band coupler with bandpass response is achieved.

The stepped-impedance resonator is capable to control all its resonant frequencies by choosing the impedance ratio K and stepped percentage α properly. In this design, the working frequencies are chosen as 1.5GHz and 2GHz. Fig. 4.47 shows the layout of the dual-band coupler.

Fig. 4.48(a) plots the simulated coupling coefficients versus the distances between resonators. As shown in Fig. 4.47, there are two parameters, d and h , which can be used to obtain required coupling coefficients. The coupling coefficients of both bands are almost the same. This property restricts the possibility of this structure. Fig. 4.48(b) plots the simulated external quality factor at first resonant frequency versus the tapped

line position and the relationship between the external quality factor of the first resonant frequency and that of the second resonant frequency. It can be observed that the ratio of external quality factors at both bands changes a lot. Because the coupling coefficients are the same at both bands, the external quality factors should be the same, too. As a result, the external quality factor Q_e is chosen as 25. The coupling coefficients are chosen as

$$M_{12} = M_{34} = 0.057$$

and

$$M_{41} = M_{23} = 0.04.$$

The design parameters shown in Fig. 4.47 are chosen as $t_1 = t_2 = t_3 = t_4 = 8.5\text{mm}$, $h_{12} = h_{34} = 0.6\text{mm}$, $h_{41} = h_{23} = 0.8\text{mm}$, $d_{12} = d_{34} = 2.5\text{mm}$, and $d_{41} = d_{23} = 3.5\text{mm}$. The circuit of this coupler is around $51\text{mm} \times 55.5\text{mm}$, i.e., $0.425\lambda \times 0.46\lambda$ (@1.5GHz).

Fig. 4.49 shows the photograph of the fabricated dual-band coupler. Fig. 4.50 and Fig. 4.51 show the simulated and measured data respectively. The comparisons of simulation and measurement are shown in Fig. 4.52, Fig. 4.53, Fig. 4.54, and Fig. 4.55. From the measured data, the return loss (S_{11}) $\geq 15\text{dB}$ in the frequency ranges of $1.5 \sim 1.525\text{ GHz}$ and $2.03 \sim 2.06\text{ GHz}$. In the first band, the magnitude of through port (S_{21}) $-4.9 \sim -5.8\text{ dB}$ and the magnitude of coupled port (S_{31}) is $-5.4 \sim -6\text{ dB}$. In the second band, the magnitude of through port (S_{21}) $-4.4 \sim -4.6\text{ dB}$ and the magnitude of coupled port (S_{31}) is $-4.3 \sim -4.6\text{ dB}$. The isolation (S_{41}) is better than 13dB in both bands. The phase difference between S_{21} and S_{31} is shown in Fig. 4.55. It has a phase difference of 90° at the first band and a phase difference of 270° at the second band.

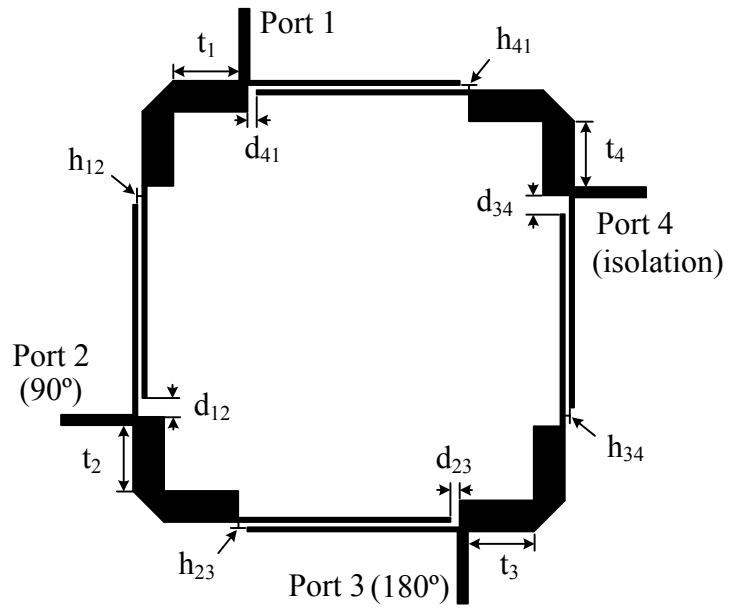


Fig. 4.47. Layout of dual-band coupler

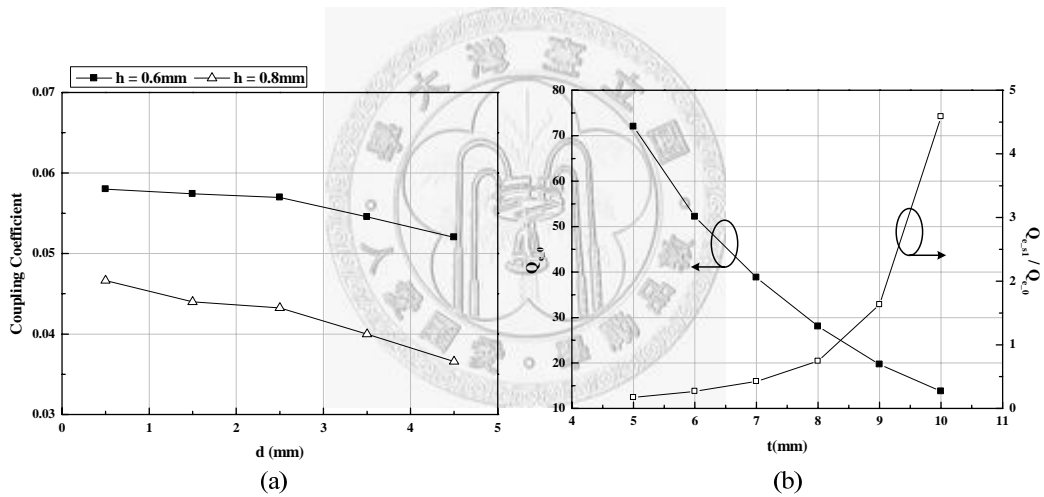


Fig. 4.48. Design features and characteristics for dual-band coupler in Fig. 4.47

(a) Coupling coefficient versus the distance between resonators

(b) External quality factor versus the tapped line position of resonator

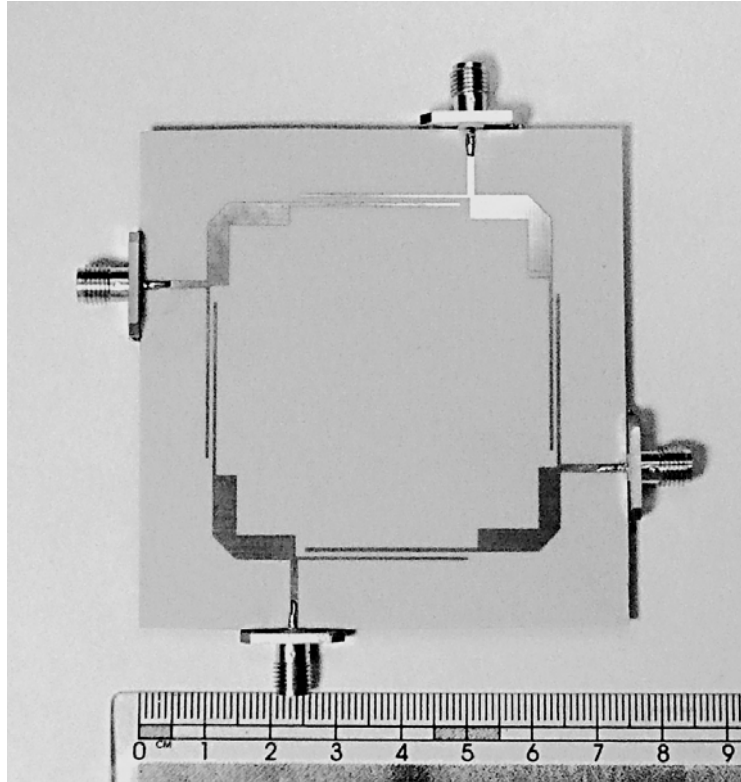


Fig. 4.49. Photograph of fabricated dual-band coupler

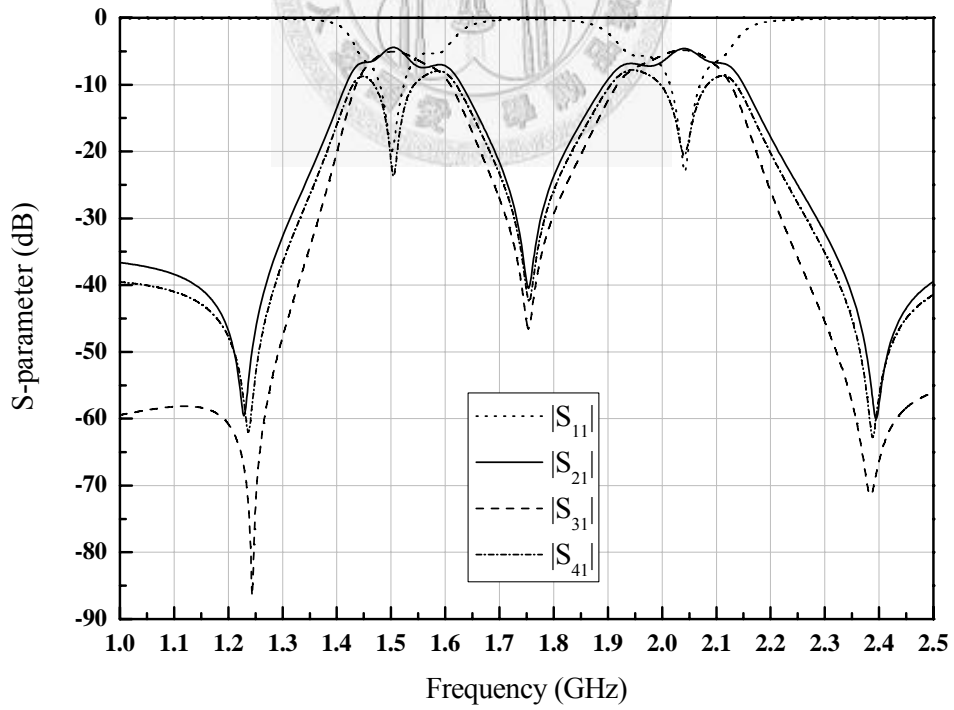


Fig. 4.50. Simulation result of dual-band coupler

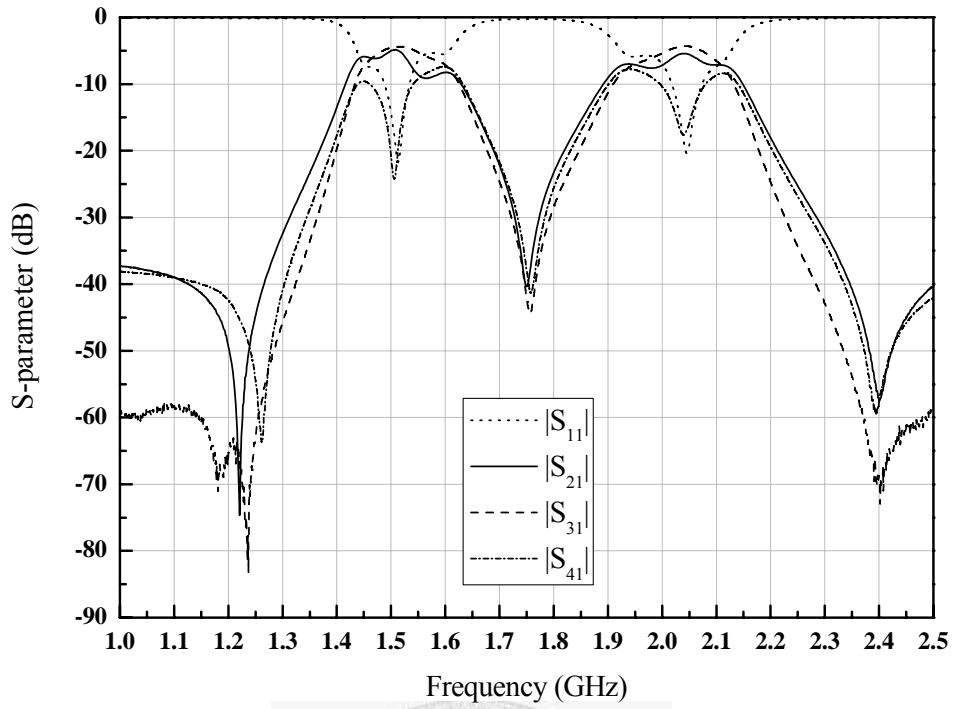


Fig. 4.51. Measurement of dual-band coupler

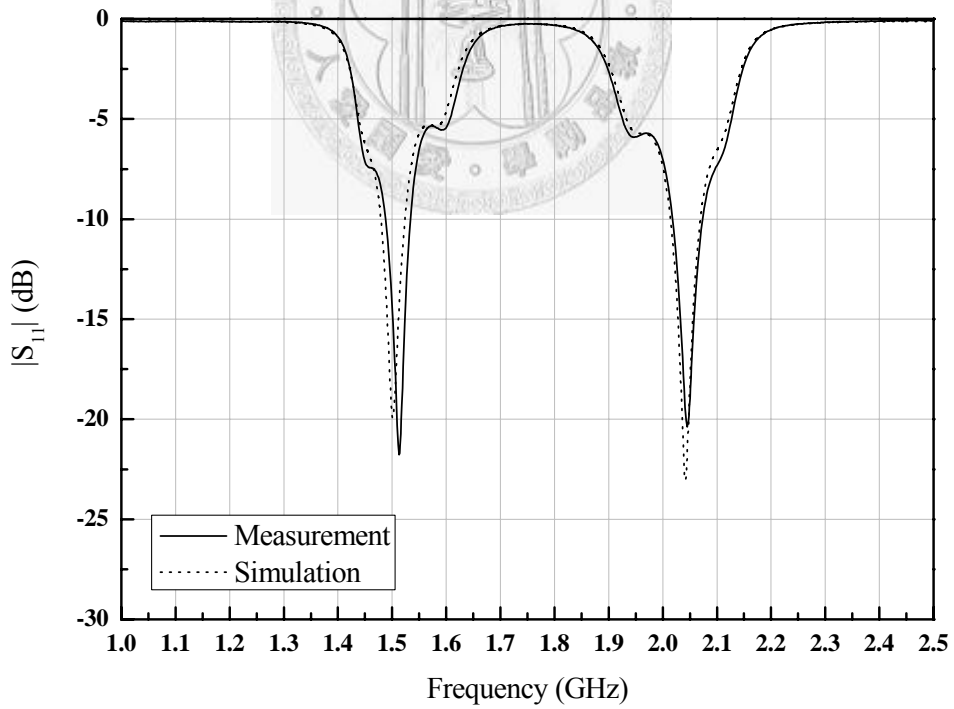


Fig. 4.52. Measured and simulated performances of dual-band coupler ($|S_{11}|$)

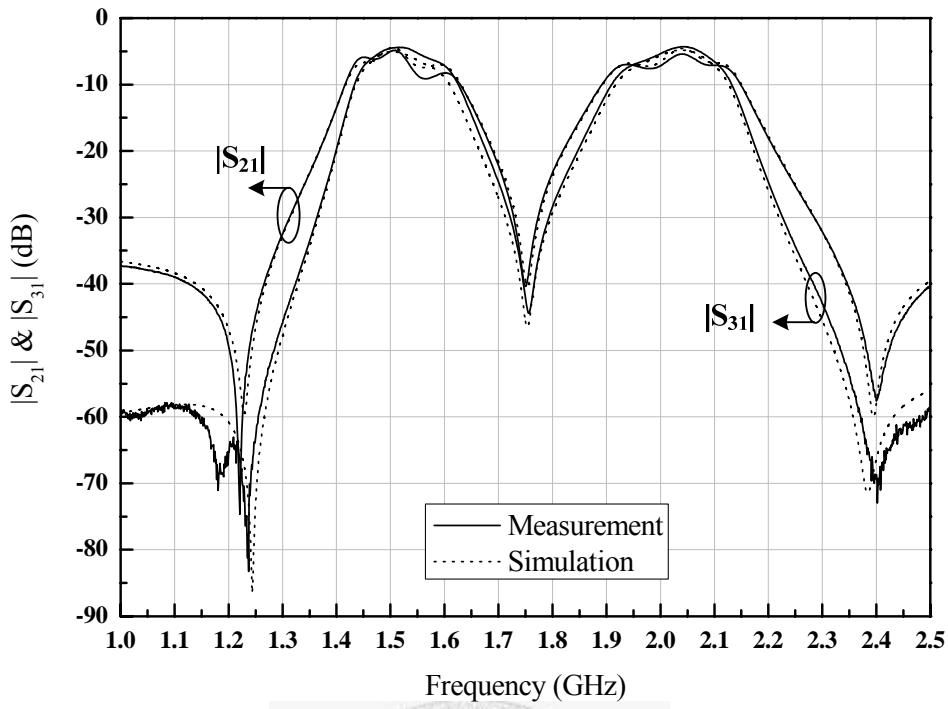


Fig. 4.53. Measured and simulated performances of dual-band coupler ($|S_{21}|$ & $|S_{31}|$)

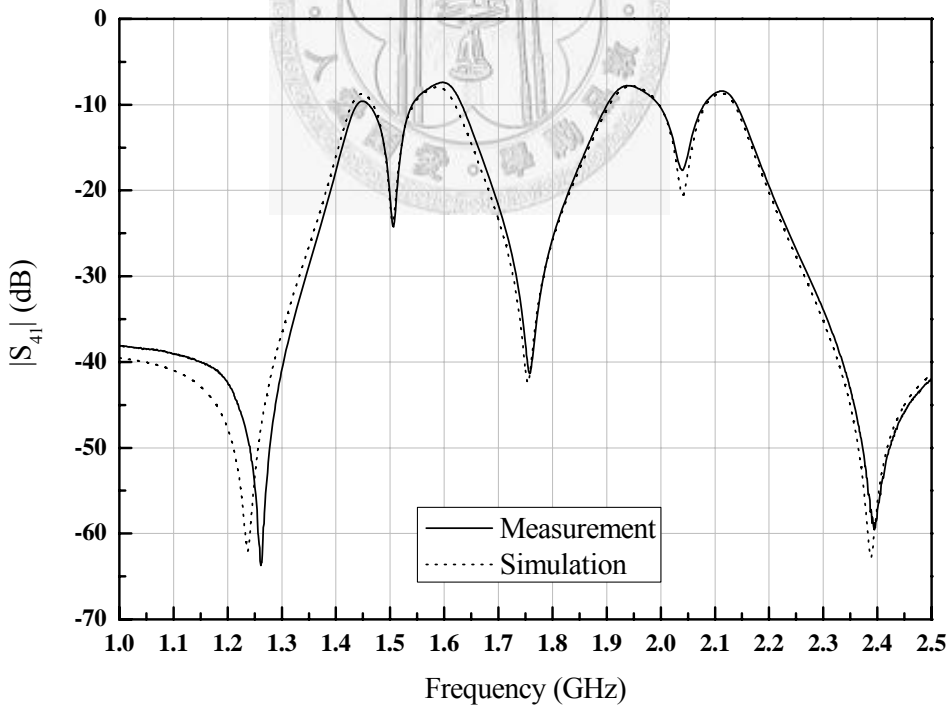


Fig. 4.54. Measured and simulated performances of dual-band coupler ($|S_{41}|$)

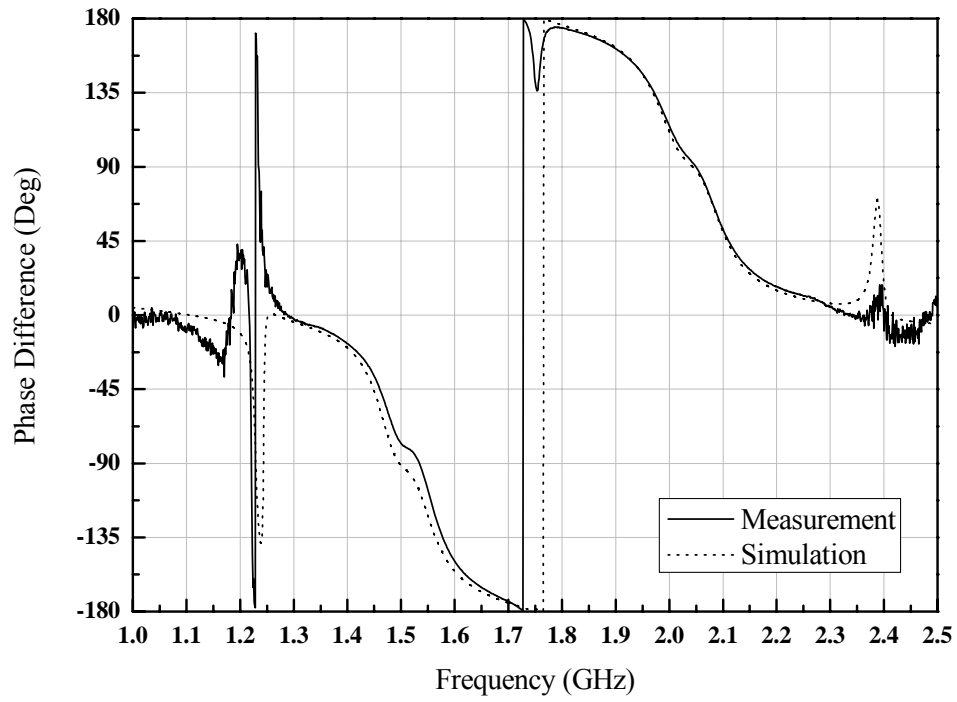
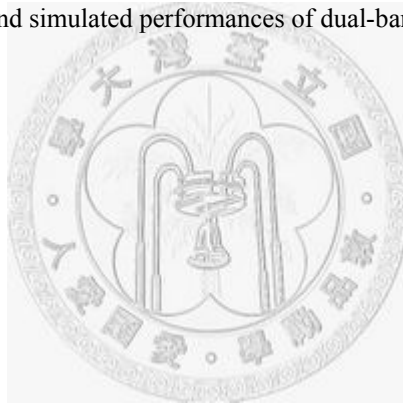


Fig. 4.55. Measured and simulated performances of dual-band coupler ($\angle S_{31} - \angle S_{21}$)



Chapter 5

Conclusions

This thesis presents compact branch-line couplers composed of coupled resonators. Because the quarter-wavelength transmission lines are equivalent to the couplings between resonators, the conventional branch-line coupler can be transformed into a coupled-resonator network. Therefore, the size of branch-line coupler reduces as the size of resonator shrinks. Besides, the coupler designed with this method has bandpass characteristics. This idea can be also applied to dual-band design.

In this thesis, the miniaturized couplers are designed and fabricated at 2GHz. This idea of transforming conventional branch-line coupler into coupled-resonator networks works well in narrow band application. With designed resonators, its size shrinks about 50% compared with conventional branch-line coupler.

This idea can be extended to dual-band design, too. With stepped-impedance resonators, a dual-band coupler can be achieved. In the thesis, a dual-band coupler designed at 1.5GHz and 2GHz is demonstrated.



References

- [1] R. K. Settaluri, G. Sundberg, A. Weisshaar, and V. K. Tripathi, "Compact folded line rat-race hybrid couplers," *IEEE Microwave Guided Wave Lett*, vol. 10, pp. 61-63, Feb. 2000.
- [2] M. Caulton, B. Hershenov, S. P. Knight, and R. E. DeBrecht, "Status of lumped elements in microwave integrated circuits---Present and future," *IEEE Trans. Microwave Theory Tech.*, vol. 19, pp. 588-599, July 1971.
- [3] T. Hirota, A. Minakawa, and M. Muraguchi, "Reduced-size branch-line and rat-race hybrids for uniplanar MMIC's," *IEEE Trans. Microwave Theory Tech.*, vol. 38, pp. 270-275, Mar. 1990.
- [4] R. K. Gupta and W. J. Getsinger, "Quasi-lumped-element 3- and 4-port networks for MIC and MMIC applications," in *IEEE MTT-S Int. Microwave Symp. Dig.*, 1984, pp. 409-411.
- [5] H. Ahn, I. S. Chang, and S. W. Yun, "Miniaturized 3-dB ring hybrid terminated by arbitrary impedances," *IEEE Trans. Microwave Theory Tech.*, vol. 42, pp. 2216-2221, Dec. 1994.
- [6] M. C. Scardelletti, G. E. Ponchak, and T. M. Weller, "Miniaturized wilkinson power dividers utilizing capacitive loading," *IEEE Microwave Wireless Comp. Lett.*, vol. 12, pp. 6-8, Jan. 2002.
- [7] C. Y. Ng, M. Chongcheawchamnan, and I. D. Robertson, "Lumped-distributed hybrids in 3D-MMIC technology," *IEE Proc. Microw., Antennas Propag.*, vol. 151, pp. 370-374, Aug. 2004.
- [8] T. N. Kuo, Y. S. Lin, C. H. Wang, and C. H. Chen, "A compact LTCC branch-line coupler using modified-T equivalent-circuit model for transmission line," *IEEE Microwave Wireless Comp. Lett.*, vol. 16, pp. 90-92, Feb. 2006.
- [9] C. C. Chen and C. K. C. Tzuang, "Synthetic quasi-TEM meandered transmission lines for compacted microwave integrated circuits," *IEEE Trans. Microwave Theory Tech.*, vol. 52, pp. 1637-1647, June 2004.
- [10] I. H. Lin, M. DeVincentis, C. Caloz, and T. Itoh, "Arbitrary dual-band components using composite right/left-handed transmission lines," *IEEE Trans. Microwave Theory Tech.*, vol. 52, no.4, pp. 1142-1149, Apr.2004
- [11] K. K. M. Cheng, and F. L. Wong, "A novel approach to the design and implementation of dual-band compact planar 90° branch-line coupler," *IEEE Trans. Microwave Theory Tech.*, vol. 52, no. 11, pp. 2458-2463, Nov. 2004

- [12] H. Uchida, N. Yoneda, Y. Konishi, and S. Makino, "Bandpass directional couplers with electromagnetically-coupled resonators," in *IEEE MTT-S Int. Microwave Symp. Dig.*, 2006, pp. 1563-1566.
- [13] J.-S. Hong and M. J. Lancaster, *Microstrip filters for RF/microwave applications*. New York: Wiley, 2001, ch. 8.
- [14] D. M. Pozar, *Microwave engineering*, 3rd ed. New York: Wiley, 2005.
- [15] M. Makimoto and S. Yamashita, "Bandpass filters using parallel coupled stripline stepped impedance resonators," *IEEE Trans. Microwave Theory Tech.*, vol. 28, pp. 1413-1417, Dec. 1980.
- [16] M. Sagawa, M. Makimoto, and S. Yamashita, "Geometrical structures and fundamental characteristics of microwave stepped-impedance resonators," *IEEE Trans. Microwave Theory Tech.*, vol. 45, pp. 1078-1085, July 1997.
- [17] C. F. Chen, T. Y. Huang, and R. B. Wu, "A miniaturized net-type microstrip bandpass filter using $\lambda/8$ resonators," *IEEE Microwave Wireless Comp. Lett., IEEE*, vol. 15, pp. 481-483, July 2005.
- [18] C. F. Chen, T. Y. Huang, and R. B. Wu, "Novel compact net-type resonators and their applications to microstrip bandpass filters," *IEEE Trans. Microwave Theory Tech.*, vol. 54, pp. 755-762, Feb. 2006.

